

Full length article

# Eocene granulite-facies metamorphism prior to deformation of the Mianhuadi mafic complex in the Ailao Shan-Red River shear zone, Yunnan Province, SW China



Ping-Ping Liu<sup>a,b,c,\*</sup>, Mei-Fu Zhou<sup>a</sup>, Guochun Zhao<sup>a</sup>, Sun-Lin Chung<sup>b,d</sup>, Wei Terry Chen<sup>e</sup>, Fei Wang<sup>c</sup>

<sup>a</sup> Department of Earth Sciences, University of Hong Kong, Hong Kong

<sup>b</sup> Institute of Earth Sciences, Academia Sinica, Taipei, Taiwan

<sup>c</sup> State Key Laboratory of Lithospheric Evolution, Institute of Geology and Geophysics, Chinese Academy of Sciences, Beijing 100029, China

<sup>d</sup> Department of Geosciences, National Taiwan University, Taiwan

<sup>e</sup> State Key Laboratory of Ore Deposit Geochemistry, Institute of Geochemistry, Chinese Academy of Sciences, Guiyang 550002, China

## ARTICLE INFO

**Keywords:**

Mianhuadi mafic complex

Granulite

Ductile deformation

Ar-Ar dating

ASRR shear zone

## ABSTRACT

The Mianhuadi mafic complex in the Ailao Shan-Red River (ASRR) shear zone, SW China, consists of granulite and mylonite, formed by granulite-facies peak metamorphism and retrograde amphibolite-facies metamorphism, with later local mylonitic deformation. Textures and mineral relics indicate that the protolith, represented by the mineral assemblage ( $M_0$ ) of olivine, clinopyroxene, plagioclase and Fe-Ti oxides, was emplaced as a mafic intrusion in the Late Permian as part of the Emeishan large igneous province. Two kinds of metamorphic mineral assemblages were identified: the peak assemblage ( $M_1$ ) of garnet + orthopyroxene + clinopyroxene + plagioclase + magnetite + ilmenite, and the retrograde assemblage ( $M_2$ ) composed of hornblende surrounding orthopyroxene and garnet, and hornblende + spinel symplectite around garnet. Pressure-temperature estimates yield 657–722 °C and 7–9 kbar, and 649–676 °C and 5–6 kbar for the  $M_1$  and  $M_2$  stages, respectively, roughly defining a clockwise P-T path with near-isothermal decompression following the peak metamorphism. These metamorphic conditions are quite unlike those (pressure up to 14 kbar) of the Late Permian-Middle Triassic metamorphic event in the region. In addition, foliated biotite from mylonites has an  $^{40}\text{Ar}$ - $^{39}\text{Ar}$  plateau age of  $34.3 \pm 0.4$  Ma, indicating that the ASRR shear zone was active at or before the Late Eocene. Combined with previous data, our new results indicate that the granulite-facies metamorphism of the Mianhuadi mafic complex occurred most likely during the Eocene, followed by rapid exhumation and ductile sinistral shearing in the Late Eocene. The formation of the granulite was likely related to the upwelling of the asthenosphere due to the delamination of overthickened lithospheric mantle after the India-Asia collision.

## 1. Introduction

In the Ailao Shan-Red River (ASRR) shear zone, gneissic massifs form a more or less continuous belt from eastern Tibet to northern Vietnam. Being one of the largest strike-slip fault zones in the world, the ASRR shear zone accommodated the northward India-Asia collision and reshaped the contours of SE Asia (e.g. Schärer et al., 1990; Harrison et al., 1992; Leloup and Kienast, 1993; Leloup et al., 1995; Chung et al., 1997; Searle, 2006; Searle et al., 2010). Numerous studies have examined the length scale of the shearing offset, the P-T conditions of metamorphism, the timing of shearing, the depth of the faults and the correlations between metamorphism and deformation in the > 1000 km long ASRR shear zone (e.g. Jolivet et al., 2001; Gilley et al., 2003; Lin et al., 2012; Liu et al., 2013; Palin et al., 2013). Although it has been

known that the metamorphic rocks along the ASRR shear zone mostly show low-grade metamorphic features attributed to left-lateral shearing in the Tertiary that is commonly accompanied by low-temperature fabrics (Schärer et al., 1990; Leloup and Kienast, 1993), recent studies show that the metamorphism locally reached upper amphibolite-facies and probably predated the Tertiary left-lateral shearing (Searle, 2006; Yeh et al., 2008; Searle et al., 2010; Lin et al., 2012; Palin et al., 2013; Wang et al., 2016).

In this study, the Mianhuadi mafic complex in the eastern part of the ASRR shear zone near the border of Yunnan province and Vietnam is recognized to have formed by granulite-facies metamorphism from a Permian layered intrusion. This complex is particularly important as the intrusive protolith formed in Permian, compared with old basement rocks as protoliths for major metamorphic rock units along the ASRR

\* Corresponding author at: Institute of Earth Sciences, Academia Sinica, Taipei 11529, Taiwan.  
E-mail address: liupingping11@live.cn (P.-P. Liu).

shear zone. This paper presents some important lines of petrographic evidence for granulite-facies metamorphism, and Ar-Ar ages of foliated biotite from mylonites. With reference to regional tectonic events, we determine the initial timing of shearing and elucidate the possible formation mechanism for the granulite-facies metamorphism around the ASRR shear zone.

## 2. Geological background

### 2.1. The Ailao Shan-Red River shear zone

The ASRR shear zone extends from the upper reaches of the Mekong River of the eastern Himalayan syntaxis, southeastwards through Yunnan province, China, to northern Vietnam. As a result of the Indian-Asian continent-continent collision, the ASRR shear zone formed during continental extrusion along tectonically weak belts on the boundary between the South China Block to the north, and the Indochina and Sibumasu blocks to the south. The shear zone is characterized by four 10–20 km wide metamorphic massifs, namely the Xuelong Shan, Diancang Shan and Ailao Shan massifs in southern China, and the Day Nui Con Voi (DNCV) massif in northern Vietnam (Fig. 1). These metamorphic massifs consist largely of mylonitic gneisses and amphibolites, with minor migmatites, mica schists and marbles (Leloup et al., 1995). The stretching of the massifs is roughly parallel to the strike of the ASRR shear zone. Kinematic and structural analyses indicate a primary left-lateral shearing in the mid-Tertiary and a subsequent right-lateral shearing in the Late Pliocene (Allen et al., 1984; Schoenbohm et al., 2006). The sinistral offset along the shear zone has been estimated to vary from 500 to 1150 km (Leloup et al., 1995). Both sides of the Red River fault zone are underlain by essentially unmetamorphosed sedimentary rocks (Leloup and Kienast, 1993). To the north, the Yangtze platform is characterized by a nearly continuous Devonian to Eocene sedimentary succession, with a few outcrops of the Yangtze platform basement. To the south of the ASRR shear zone lies the Simao basin with Silurian to Eocene strata.

Detrital zircons from paragneisses of the four metamorphic massifs in the ASRR shear zone record multiple episodes of magmatism between Neoarchean and Neoproterozoic (Lin et al., 2012; Liu et al., 2013). The magmatic rocks along the ASRR shear zone were dated to be ~240 Ma and 40–25 Ma (Chung et al., 1997; Lin et al., 2012). The metamorphic conditions in the four massifs were suggested to be low-grade with estimated P-T at 3–7 kbar and 550–780 °C (Leloup et al., 1995; Leloup and Kienast, 1993), whereas recent studies revealed that the peak metamorphic conditions reached 720–760 °C or even ~805 °C and 8.0–9.6 kbar during Eocene and Oligocene (Liu et al., 2013; Palin et al., 2013). Recent studies also indicated that there was an earlier stage of high-pressure metamorphism during the Early-Middle Triassic (Liu et al., 2013), broadly coeval with the high-temperature metamorphic event that affected the basement of Vietnam (Carter et al., 2001). The geological complexity of the massifs along the ASRR shear zone mainly resulted from the amalgamation and accretion of the Gondwana-derived terranes in SE Asia, and the final collision of India with Asia that led to metamorphism and displacement (Metcalfe, 1995).

### 2.2. The Mianhuadi mafic complex

The Mianhuadi mafic complex is located between the Ailaoshan and DNCV massifs, near Jinping county of southernmost Yunnan Province and close to the northern border of Vietnam (Fig. 1). The elongated mafic complex extends NW-SE along the ASRR shear zone, and was apparently deformed by the shearing. Igneous zircon with a U-Pb age of  $259.6 \pm 0.8$  Ma has been reported for the Mianhuadi mafic complex and the age was taken as the emplacement age of the magmatic protolith (Zhou et al., 2013). The Mianhuadi mafic complex is hosted in amphibole-plagioclase gneisses, biotite-plagioclase gneisses, plagioclase amphibolites and migmatites of the Proterozoic Ailaoshan Group.

The Mianhuadi mafic complex also underwent varying degrees of metamorphism and/or deformation with primary gabbroic textures locally preserved. Granulite and mylonite are the major rock types in the Mianhuadi mafic complex, where three Fe-Ti oxide orebodies, namely the Ma'anshan, Wanhe and Dapo bodies, were hosted (Fig. 2). The primary igneous rocks that comprise the Mianhuadi mafic complex include clinopyroxenite, gabbro, olivine gabbro, (Fe-Ti) oxide gabbro and (Fe-Ti) oxide ores.

## 3. Petrography

Petrological examination has shown that the Mianhuadi mafic complex is highly variable in terms of degree of metamorphism and deformation. Based on the extent of mylonitization, rocks of the Mianhuadi mafic complex can largely be classified into two groups: (1) partially recrystallized, undeformed rocks with delicate corona textures that are composed of hornblende, orthopyroxene, garnet and a variety of symplectites; and (2) fully recrystallized and foliated rocks characterized by medium-grained oriented hornblende and biotite crystals.

Garnet and orthopyroxene were only observed in two (out of twelve) samples. Anorthite + hornblende and hornblende + spinel symplectites are delicately preserved in undeformed rocks, whereas in the highly deformed rocks they were replaced by elongated and oriented hornblende and biotite. Cumulus textures of euhedral silicate minerals and interstitial Fe-Ti oxides preserved in some of the granulites of the Mianhuadi mafic complex (Fig. 3A and B) indicate that the protolith was a Fe-Ti oxide-bearing mafic-ultramafic intrusion. Igneous relics including olivine, clinopyroxene, plagioclase, magnetite, ilmenite and spinel together are identified as the protolith assemblage ( $M_0$ ). On the basis of microstructures and reaction relations among the mineral phases, two mineral assemblages of metamorphism have been recognized: a peak metamorphic assemblage ( $M_1$ ), and a retrograde metamorphic assemblage ( $M_2$ ). Later deformation (mylonitization) was superimposed on a portion of the metamorphosed rocks.

### 3.1. Peak assemblage ( $M_1$ )

The peak metamorphic stage ( $M_1$ ) preserved in the Mianhuadi mafic complex is represented by the growth of garnet and fine-grained orthopyroxene, and indicates intermediate-pressure granulite facies conditions (Green and Ringwood, 1967). Two types of garnets were observed. One occurs as polygonal grains replacing plagioclase and surrounded by anorthite + hornblende (symplectites) (Fig. 3C and D). The other occurs as an inner shell surrounding plagioclase, mantled by an outer shell of hornblende (Fig. 3E). Orthopyroxene occurs rarely as hexagonal but commonly irregularly shaped or fan-shaped columnar aggregates replacing the border of olivine (Fig. 3G). Locally, the olivine is mantled by an outer, ~100 µm wide shell of fine-grained, fan-shaped hornblende aggregates that embayed the olivine relics (Fig. 3G).

### 3.2. Retrograde assemblage ( $M_2$ )

Anorthite + hornblende symplectites are locally present in the plagioclase-rich rocks of the Mianhuadi mafic complex. They represent the early  $M_2$  metamorphic stage following peak metamorphism ( $M_1$ ). The symplectitic texture consists of fine-grained, worm-like anorthite + hornblende coronas around embayed igneous plagioclase relics (Fig. 3F). The anorthite + hornblende symplectitic corona is invariably located adjacent to the plagioclase relics and is mantled by the hornblende + spinel symplectites (Fig. 3F and H), suggesting that the former developed later than the hornblende + spinel symplectitic corona, i.e., during retrograde metamorphism. In most cases, hornblende + spinel symplectites completely pseudomorph laths of plagioclase.

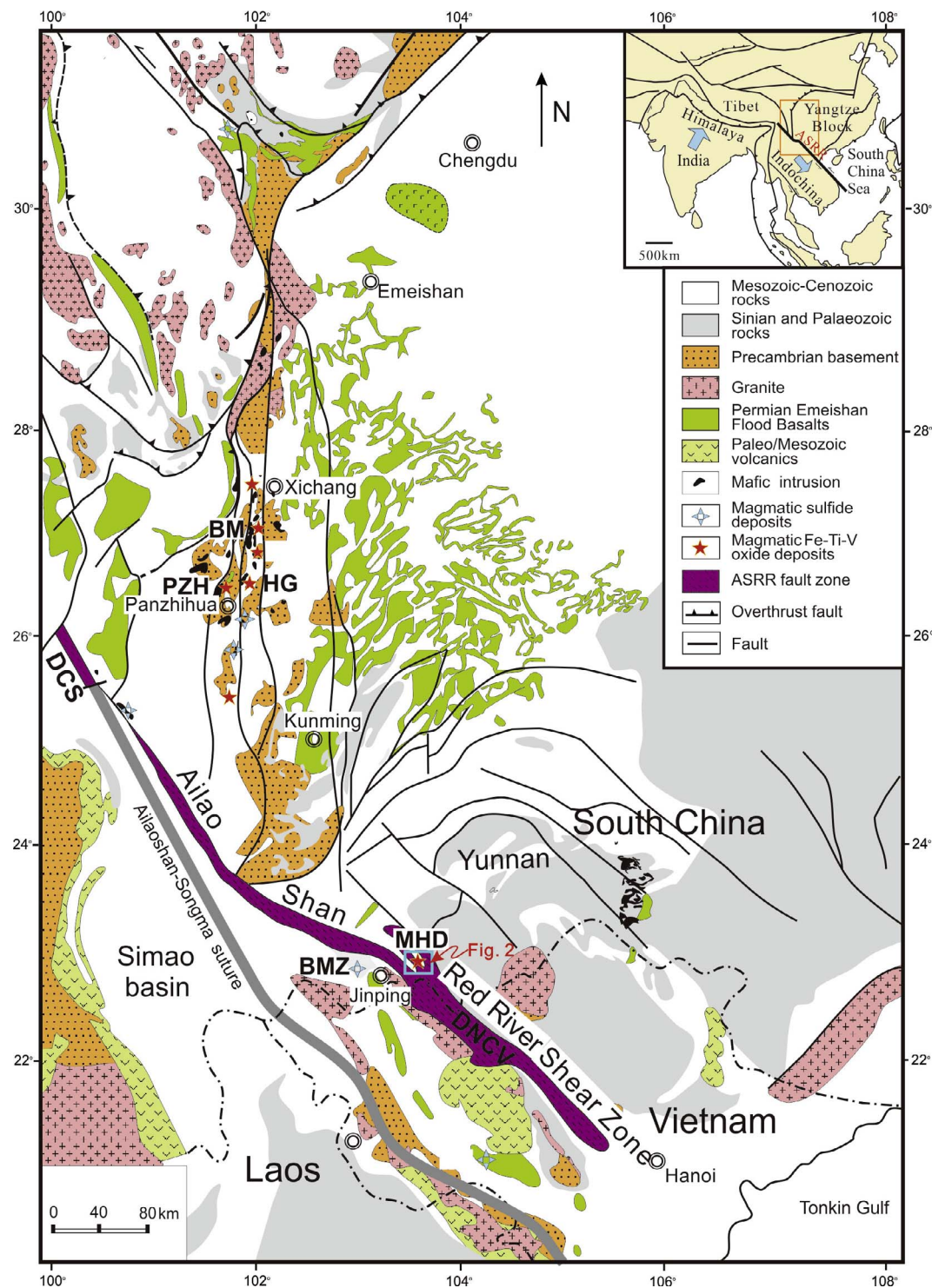


**Fig. 1.** A simplified geological map of SW China and northern Vietnam, showing the major lithotectonic units of the ASRR shear zone and flood basalts/intrusions of the ELIP distributed in the north and south of the ASRR shear zone (modified from Wang et al., 2007). Abbreviations of major magmatic mafic-ultramafic intrusions: BM, Baimazhai; HG, Hongge; PZH, Panzhihua; MHD, Mianhuadi; BMZ, Baimazhai. Metamorphic massifs along the ASRR shear zone: DCS, Diancang Shan; DNCV, Day Nui Con Voi.

### 3.3. Mylonitization

Mylonites from the Mianhuadi mafic complex are characterized by (1) presence of abundant silicates of hornblende and biotite completely replacing olivine, clinopyroxene, plagioclase and various symplectic textures; and (2) orientation of hornblende and biotite in the same direction with the foliation of the rocks (Fig. 4A and B). The mylonitization may have occurred after the main metamorphic stages given the lack of symplectic textures and peak stage minerals in these strongly

deformed rocks. Some rocks with granulite-facies minerals and textures did not undergo mylonitization and deformation.

## 4. Analytical methods

### 4.1. Mineral compositions

Major element compositions of silicate minerals were determined by wavelength-dispersive spectrometry using a JEOL JXA8100 electron

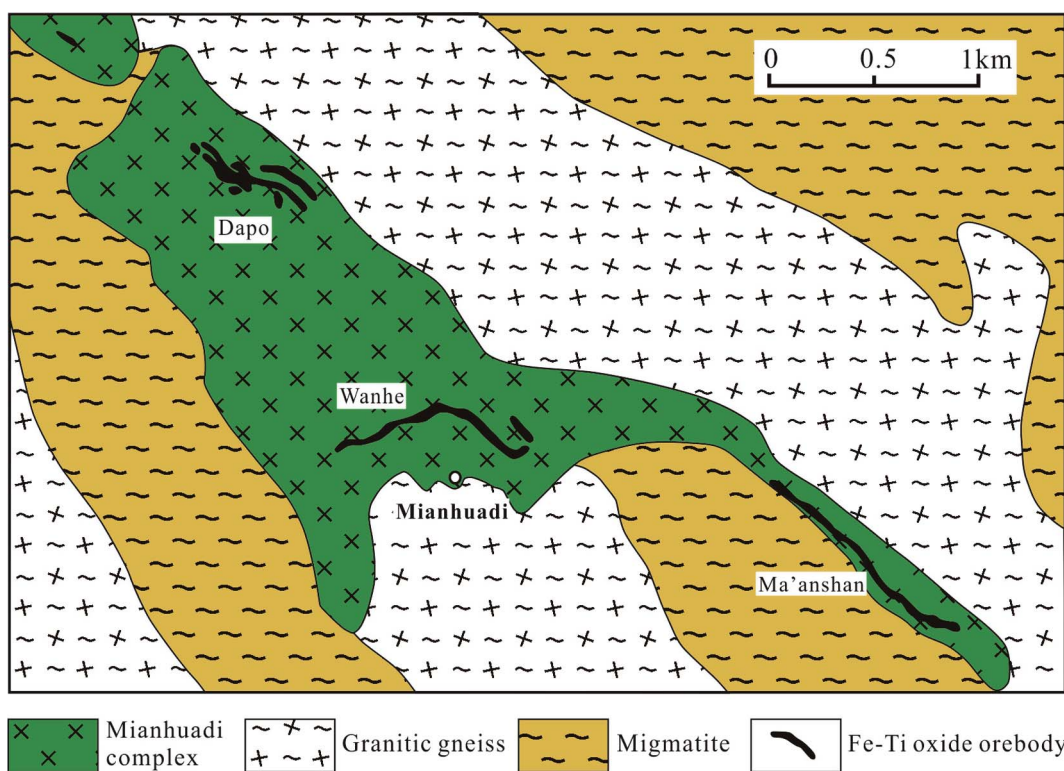


**Fig. 2.** A simplified geological map of the Mianhuadi mafic complex in the ASRR shear zone, showing the distribution of the Dapo, Wanhe and Ma'anshan orebodies, modified after Peng (2009).

microprobe (EMP) at Institute of Geology and Geophysics, Chinese Academy of Sciences (IGGCAS). The electron microprobe was operated under an accelerating voltage of 15 kV and a beam current of 12 nA, using a beam spot of 5  $\mu\text{m}$  and counting time of 10 to 30 s. Minerals and synthetic oxides were used as standards. A program based on the ZAF procedures was used for data correction. The precisions of all analyzed elements were better than 1.5%.

#### 4.2. Ar-Ar dating of biotite

Biotite from sample MS11 was handpicked for  $^{40}\text{Ar}/^{39}\text{Ar}$  analyses. The biotite separates were wrapped in aluminum foil to form wafers, and stacked in quartz vials with the international standard YBCs ( $29.286 \pm 0.045$  Ma; Wang et al., 2014). Neutron irradiation was carried out in position H8 of 49-2 Nuclear Reactor (49-2 NR), Beijing (China), with a flux of  $\sim 6.5 \times 10^{12} \text{n} (\text{cm}^2 \text{s})^{-1}$  for 24 h. A CO<sub>2</sub> laser fusion technique was used for  $^{40}\text{Ar}/^{39}\text{Ar}$  analyses.

Isotopic measurements were made using the Noblesse mass spectrometer at the IGGCAS. The correction factors for Ca and K were  $[^{36}\text{Ar}/^{37}\text{Ar}]_{\text{Ca}} = 0.000261 \pm 0.0000142$ ,  $[^{39}\text{Ar}/^{37}\text{Ar}]_{\text{Ca}} = 0.000242 \pm 0.0000281$ ,  $[^{40}\text{Ar}/^{39}\text{Ar}]_{\text{K}} = 0.00088 \pm 0.000023$ . The ages were calculated using the decay constant ( $5.543 \times 10^{-10} \text{ yr}^{-1}$ ) proposed by Steiger and Jäger (1977) and all errors were quoted at the  $2\sigma$  level.

Plateau ages were determined from three or more contiguous steps, comprising > 50% of the  $^{39}\text{Ar}$  released, and revealed concordant ages at the 95% confidence level. Because no assumption was made regarding the trapped component, the preferred age is the isochron age, calculated from the results of plateau steps using the York regression algorithm (York, 1969).

The age errors reported here are internal errors, including analytical error and errors on blank, interaction factor, mass-discrimination and J-value. The error on the total decay constant was not propagated into the age error. Uncertainties on all data reported herein are at the 95%

confidence level ( $2\sigma$ ). The data were processed by using ArArCALC (Koppers, 2002).

## 5. Results

### 5.1. Mineral chemistry

#### 5.1.1. Garnet

Both euhedral polygonal garnet replacing plagioclase, and anhedral garnet growing around plagioclase are dominated by almandine ( $X_{\text{Alm}} = 0.52\text{--}0.61$ ), pyrope ( $X_{\text{Prp}} = 0.18\text{--}0.26$ ) and grossular ( $X_{\text{Grs}} = 0.13\text{--}0.27$ ), with minor andradite ( $X_{\text{Adr}} = 0\text{--}0.05$ ) and spessartine ( $X_{\text{Spa}} = 0.01\text{--}0.02$ ) (Table 1). The euhedral garnet grains exhibit weak core to rim compositional zoning in terms of FeO and MnO contents (Fig. 5A). Anhedral garnet crystals around plagioclase also display compositional variations depending on whether they are in contact with plagioclase or hornblende.

#### 5.1.2. Clinopyroxene

The clinopyroxene crystals from all the studied samples represent igneous relics preserved due to incomplete metamorphic reactions. They are augite or diopside with variable En (37.7 to 54.9), Fs (5.8 to 13.5) and Wo (34.3 to 53.9) contents, similar to clinopyroxene in Fe-Ti oxide-bearing layered mafic-ultramafic intrusions of the ELIP (Table 2). The heterogeneous compositions of individual clinopyroxene grains might be due to the modification by retrograde metamorphism and fluid alteration, which is evidenced by the covariation of increasing Al<sub>2</sub>O<sub>3</sub> and CaO with decreasing SiO<sub>2</sub> that likely records clinopyroxene-hornblende retrograde transition.

#### 5.1.3. Orthopyroxene

Granular and radial orthopyroxene crystals replaced olivine in several samples. Olivine relics in samples DP22 and DP15 have Fo values from 68 to 70 and 59 to 61, respectively, with corresponding high-

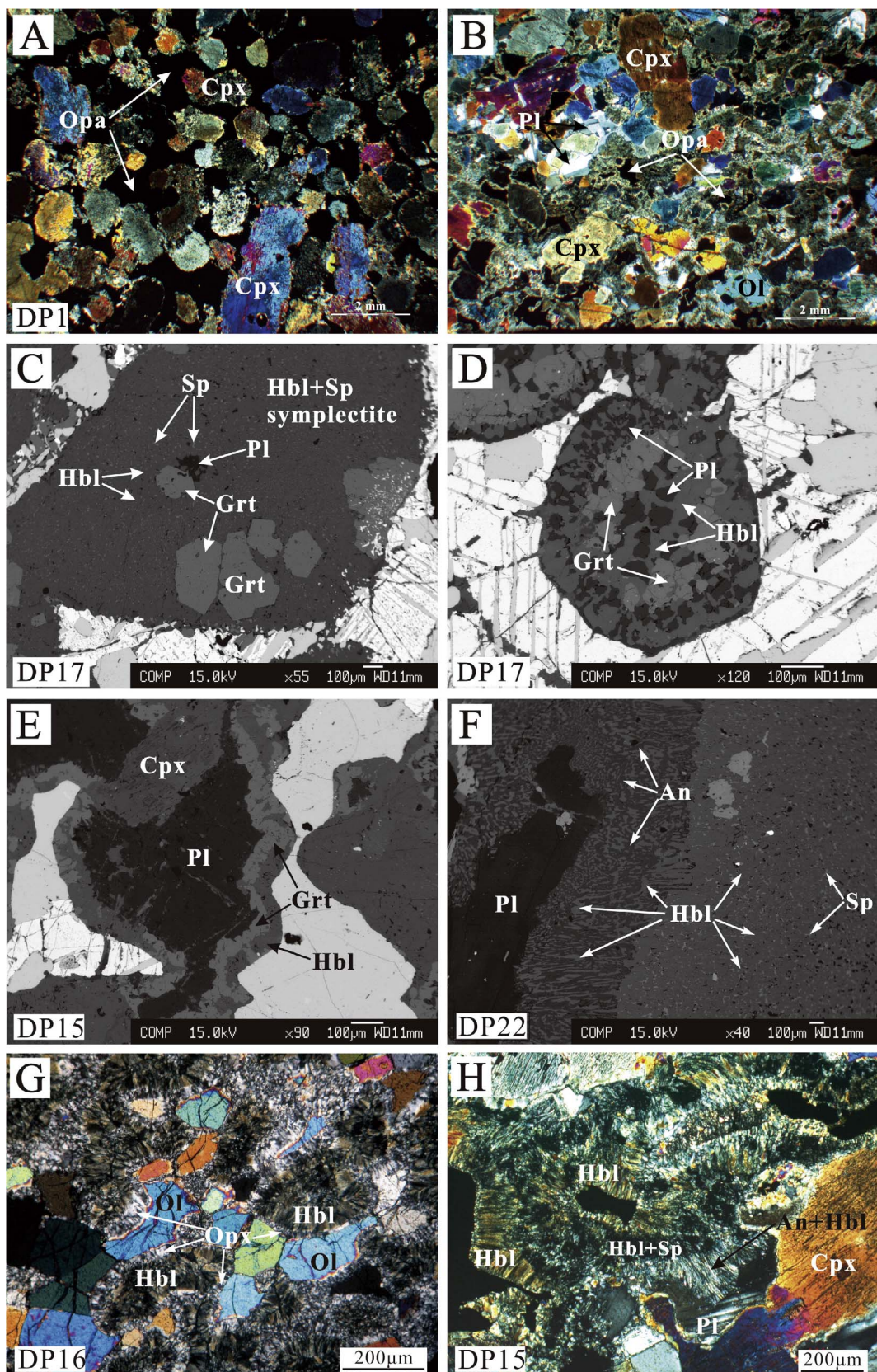


**Fig. 3.** Photomicrographs showing representative metamorphic reaction textures of the rocks studied. A. Cumulus silicates, dominated by clinopyroxene (Cpx), and interstitial opaque (Opa) minerals of Fe-Ti oxides. B. Fe-Ti oxide-bearing gabbro consisting of cumulus olivine (Ol), clinopyroxene, plagioclase (Pl) and interstitial opaque minerals of Fe-Ti oxides. C. Plagioclase relic and newly formed polygonal garnet (Grt) within hornblende (Hbl) + spinel (Sp) symplectite (BSE image). D. Anhedral garnet crystals in contact with plagioclase and hornblende (BSE image). E. Plagioclase surrounded by an inner shell of garnet and an outer shell of hornblende (BSE image). F. Plagioclase core surrounded by an inner rim of anorthite (An) + hornblende symplectite and an outer rim of hornblende + spinel symplectite (BSE image). G. Olivine surrounded by an inner shell of fine-grained orthopyroxene (Opx) aggregates and an outer shell of ~100 µm wide layer of fine-grained fan-shaped aggregates of hornblende (cross-polarized light). H. Plagioclase (An = 65–75) replaced by an inner shell of anorthite + hornblende and an outer shell of hornblende + spinel (cross-polarized light).

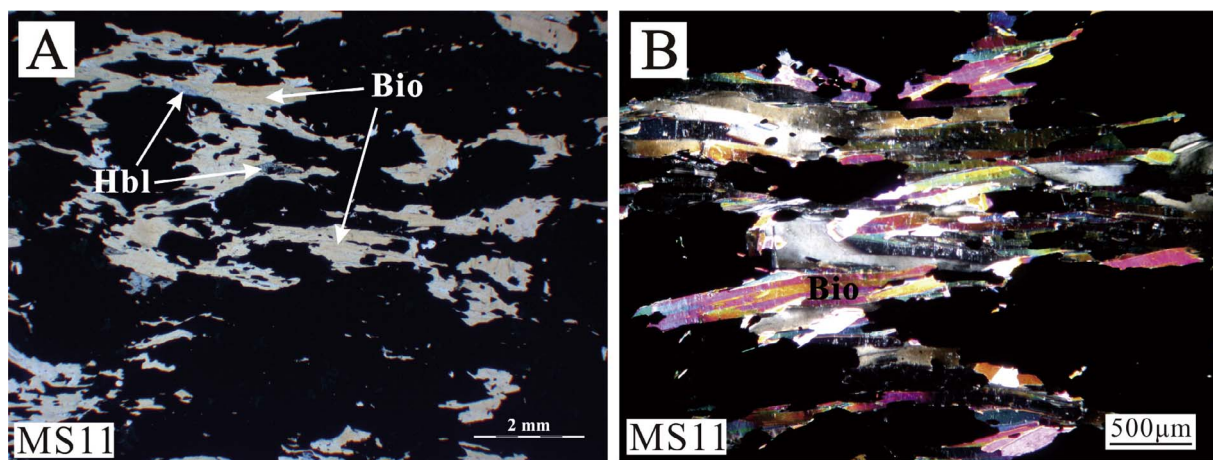


**Fig. 4.** A photomicrograph of the mylonite from the Mianhuadi mafic complex showing the foliation and orientation of biotite (Bio) and hornblende (Hbl) under plane-polarized light (A) and cross-polarized light (B).

Mg orthopyroxene ( $\text{Mg} \# = 73$  to  $74$ ) in sample DP22 and low-Mg orthopyroxene ( $\text{Mg} \# = 68$  to  $71$ ) in sample DP15 (Table 3). This indicates that the composition of the newly formed orthopyroxene was determined by the composition of the former igneous olivine.

#### 5.1.4. Plagioclase

The relict plagioclase laths in the Mianhuadi mafic complex are generally zoned with increasing then decreasing An contents (from  $\text{An}_{66}$  to  $\text{An}_{72}$  to  $\text{An}_{68}$ ) from the core to rim (Fig. 5B, Table 4). The symplectitic anorthite in the granulite of the Mianhuadi mafic complex has remarkably high  $\text{CaO}$  and low  $\text{Na}_2\text{O}$  contents ( $\text{An} = 83$  to  $96$ ) compared with the igneous plagioclase relics in contact (Fig. 5C). This compositional heterogeneity is expected if incomplete metamorphic reactions and local equilibrium occurred.

**Table 1**  
Representative EMP analyses of garnet.

Sample Texture	DP15					DP17							
	Anhedral					Polygonal							
Point	1	2	3	4	5	Rim-core-rim							
$\text{SiO}_2$	39.1	38.9	38.6	39.2	37.5	38.8	38.9	37.9	38.1	38.7	38.6	39.5	38.7
$\text{TiO}_2$	0.05	0.05	0.07	0.03	1.57	0.00	0.02	0.01	0.04	0.00	0.05	0.03	0.02
$\text{Al}_2\text{O}_3$	21.9	22.1	21.6	22.1	21.2	22.3	22.1	22.9	21.6	21.9	21.8	22.6	21.7
$\text{FeO}$	24.3	24.5	24.9	24.6	26.7	27.9	27.8	28.3	28.6	28.6	28.2	28.2	27.8
$\text{MnO}$	0.65	0.69	0.80	0.58	0.99	0.94	0.62	0.65	0.59	0.57	0.62	0.63	0.95
$\text{MgO}$	4.89	5.01	5.57	4.64	4.75	6.52	6.15	6.28	6.22	6.45	6.36	6.60	6.61
$\text{CaO}$	9.86	9.79	8.56	9.73	7.95	5.21	5.84	5.25	4.90	4.84	5.05	5.06	4.97
$\text{Na}_2\text{O}$	0.07	0.03	0.08	0.10	0.04	0.02	0.02	0.00	0.05	0.00	0.02	0.03	0.07
$\text{K}_2\text{O}$	0.01	0.01	0.02	0.00	0.02	0.01	0.00	0.00	0.02	0.00	0.00	0.00	0.01
Total	100.9	101.1	100.2	100.9	100.8	101.6	101.4	101.3	100.1	101.1	100.7	102.7	100.8
Si	3.01	2.99	2.99	3.01	2.92	2.97	2.99	2.92	2.97	2.99	2.99	3.00	2.99
Ti	0.00	0.00	0.00	0.00	0.09	0.00	0.00	0.00	0.00	0.00	0.00	0.00	0.00
Al	1.99	2.00	1.97	2.01	1.95	2.01	2.00	2.07	1.98	1.99	1.99	2.01	1.97
$\text{Fe}^{3+}$	0.00	0.02	0.05	0.00	0.02	0.06	0.03	0.10	0.07	0.03	0.03	0.00	0.06
$\text{Fe}^{2+}$	1.56	1.56	1.56	1.58	1.72	1.73	1.76	1.72	1.79	1.81	1.79	1.79	1.73
Mn	0.04	0.04	0.05	0.04	0.07	0.06	0.04	0.04	0.04	0.04	0.04	0.04	0.06
Mg	0.56	0.57	0.64	0.53	0.55	0.74	0.70	0.72	0.72	0.74	0.73	0.74	0.76
Ca	0.81	0.81	0.71	0.80	0.66	0.43	0.48	0.43	0.41	0.40	0.42	0.41	0.41
Na	0.01	0.00	0.01	0.02	0.01	0.00	0.00	0.00	0.01	0.00	0.00	0.00	0.01
K	0.00	0.00	0.00	0.00	0.00	0.00	0.00	0.00	0.00	0.00	0.00	0.00	0.00
Total	8.0	8.0	8.0	8.0	8.0	8.0	8.0	8.0	8.0	8.0	8.0	8.0	8.0
$X_{\text{Alm}}$	0.52	0.52	0.53	0.54	0.57	0.58	0.59	0.59	0.60	0.61	0.60	0.60	0.58
$X_{\text{Sp}}_{\text{s}}$	0.01	0.02	0.02	0.01	0.02	0.02	0.01	0.01	0.01	0.01	0.01	0.01	0.02
$X_{\text{Prp}}$	0.19	0.19	0.22	0.18	0.18	0.25	0.24	0.25	0.24	0.25	0.25	0.25	0.26
$X_{\text{Grs}}$	0.27	0.27	0.24	0.27	0.22	0.14	0.16	0.15	0.14	0.13	0.14	0.14	0.14
$X_{\text{Adr}}$	0.00	0.01	0.03	0.00	0.01	0.03	0.02	0.05	0.04	0.02	0.02	0.00	0.03

#### 5.1.5. Spinel

Spinel from the Mianhuadi mafic complex belongs to the spinel-hercynite series. In a single sample, sample DP22 for example, symplectitic spinel has high Mg# (47.1 to 50.4) and  $\text{Al}_2\text{O}_3$  contents (61.4 to 63.6 wt.%), both of which exhibit a linear correlation. Granular spinel in intersitital Fe-Ti oxides and that replacing olivine have a similarly lower Mg# and  $\text{Al}_2\text{O}_3$  contents and higher  $\text{Cr}_2\text{O}_3$  contents than the symplectitic spinel (Table 5). Overall, the granular spinel in the Mianhuadi mafic complex has low Mg# values and displays a wider compositional range than the other varieties (Fig. 5D).

#### 5.1.6. Hornblende

The representative chemical compositions of the various types of hornblende are presented in Table 6. All the hornblende crystals are

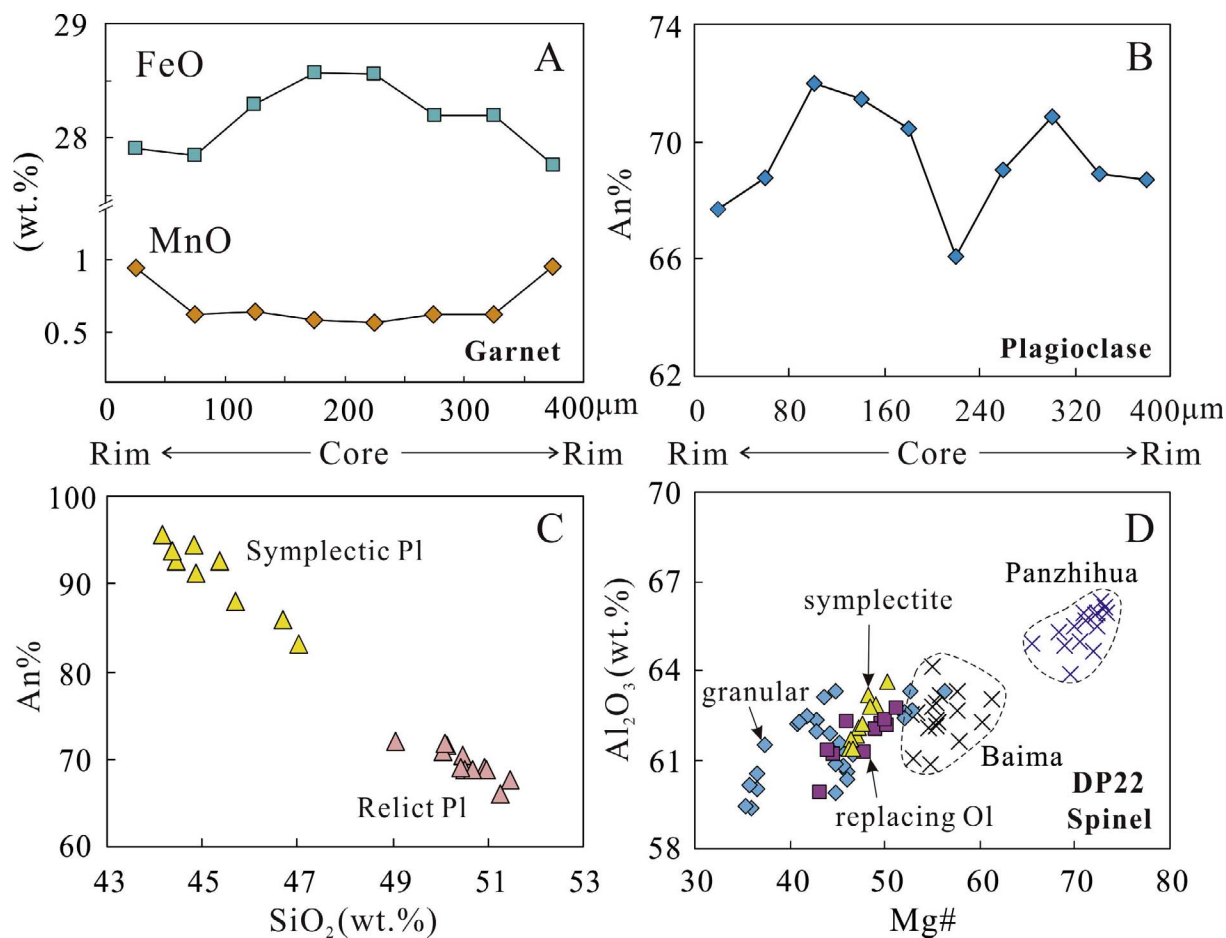


Fig. 5. Compositional variations of garnet, plagioclase and spinel from the Mianhuadi mafic complex.

calcic but highly variable in composition and classified as magnesioc-sadanagaite, pargasite and magnesiohornblende. Symplectic and medium-grained prismatic hornblende crystals are pargasite and do not show compositional differences with an exception that hornblende from

hornblende + anorthite symplectites has lower Mg# than medium-grained prismatic hornblende. Mg# increases systematically from symplectic hornblende with anorthosite, through prismatic hornblende in deformed rocks to symplectic hornblende with spinel (Fig. 6).

**Table 2**  
Representative EMP analyses of clinopyroxene.

Sample	DP1					DP15					
	Point	1	2	3	4	5	Rim-core-rim profile				
SiO <sub>2</sub>	51.6	52.0	53.7	53.2	53.8	51.2	52.1	52.3	53.0	51.5	50.4
TiO <sub>2</sub>	0.45	0.65	0.33	0.54	0.22	0.39	0.76	0.54	0.31	0.77	0.94
Al <sub>2</sub> O <sub>3</sub>	4.31	3.59	1.62	2.53	1.28	4.67	2.81	2.88	2.31	2.85	4.04
FeO	5.11	4.28	3.82	3.66	4.13	4.62	4.64	4.21	4.31	7.32	8.05
MnO	0.17	0.11	0.13	0.10	0.13	0.14	0.15	0.16	0.11	0.16	0.25
MgO	15.8	15.2	15.7	15.6	15.8	15.9	15.4	15.2	16.0	14.4	13.7
CaO	21.3	23.3	24.3	24.4	24.3	20.8	23.0	23.6	22.8	21.7	21.2
Na <sub>2</sub> O	0.30	0.16	0.04	0.05	0.05	0.40	0.12	0.08	0.16	0.29	0.49
Total	99.0	99.3	99.6	100.1	99.8	98.1	99.0	98.9	99.1	99.0	99.2
Si	7.62	7.67	7.89	7.77	7.90	7.60	7.72	7.74	7.82	7.70	7.56
Ti	0.05	0.07	0.04	0.06	0.02	0.04	0.08	0.06	0.03	0.09	0.11
Al	0.75	0.62	0.28	0.44	0.22	0.82	0.49	0.50	0.40	0.50	0.71
Fe <sup>T</sup>	0.63	0.53	0.47	0.45	0.51	0.57	0.57	0.52	0.53	0.92	1.01
Mn	0.02	0.01	0.02	0.01	0.02	0.02	0.02	0.02	0.01	0.02	0.03
Mg	3.47	3.34	3.43	3.40	3.46	3.53	3.41	3.36	3.52	3.21	3.06
Ca	3.37	3.68	3.82	3.82	3.83	3.30	3.65	3.74	3.60	3.48	3.41
Na	0.09	0.04	0.01	0.02	0.01	0.12	0.03	0.02	0.05	0.08	0.14
Total	16.0	16.0	15.9	16.0	16.0	16.0	16.0	16.0	16.0	16.0	16.0
En%	46.4	44.3	44.5	44.3	44.4	47.7	44.7	44.1	46.0	42.2	40.9
Fs%	8.4	7.0	6.1	5.8	6.5	7.7	7.5	6.8	6.9	12.0	13.5
Wo%	45.1	48.7	49.5	49.8	49.1	44.6	47.8	49.1	47.0	45.8	45.6
Mg#	84.6	86.4	88.0	88.4	87.2	86.0	85.6	86.6	86.9	77.8	75.2

**Table 3**

Representative EMP analyses of orthopyroxene.

Sample	DP22								DP15				
Texture	Granular Opx replacing the rim of Ol								Radial Opx aggregates replacing Ol				
Point	1	2	3	4	5	6	7	8	1	2	3	4	5
SiO <sub>2</sub>	54.7	54.6	55.0	53.9	54.7	54.6	54.6	54.6	55.1	53.7	55.2	54.1	52.6
TiO <sub>2</sub>	0.02	0.03	0.03	0.04	0.02	0.08	0.10	0.08	0.03	—	—	—	0.01
Al <sub>2</sub> O <sub>3</sub>	1.29	1.67	1.42	1.71	1.45	1.15	2.35	2.22	1.94	1.24	0.80	0.37	1.04
FeO	16.7	16.9	17.1	16.4	17.5	16.9	17.3	17.4	19.1	20.0	19.3	20.2	19.6
MnO	0.39	0.38	0.42	0.41	0.45	0.40	0.44	0.38	0.23	0.33	0.34	0.31	0.29
MgO	26.8	26.8	26.7	26.4	26.5	26.8	26.6	26.4	26.7	24.7	25.9	24.7	24.7
CaO	0.10	0.12	0.10	0.11	0.15	0.18	0.10	0.09	0.51	0.21	0.21	0.16	0.23
Total	100.0	100.4	100.7	99.0	100.8	100.1	101.5	101.2	103.6	100.1	101.8	99.8	98.5
Si	1.98	1.97	1.97	1.97	1.97	1.97	1.95	1.95	1.94	1.97	1.98	1.99	1.96
Ti	0.00	0.00	0.00	0.00	0.00	0.00	0.00	0.00	0.00	—	—	—	0.00
Al	0.06	0.07	0.06	0.07	0.06	0.05	0.10	0.09	0.08	0.05	0.03	0.02	0.05
Fe	0.51	0.51	0.51	0.50	0.53	0.51	0.52	0.52	0.56	0.61	0.58	0.62	0.61
Mn	0.01	0.01	0.01	0.01	0.01	0.01	0.01	0.01	0.01	0.01	0.01	0.01	0.01
Mg	1.44	1.44	1.43	1.44	1.42	1.44	1.42	1.41	1.40	1.35	1.38	1.35	1.38
Ca	0.00	0.00	0.00	0.00	0.01	0.01	0.00	0.00	0.02	0.01	0.01	0.01	0.01
Total	4.00	4.00	3.99	4.00	4.00	4.00	4.00	4.00	4.02	4.00	4.00	4.00	4.01
Mg#	74.0	73.9	73.6	74.1	72.9	73.9	73.3	73.0	71.4	68.8	70.5	68.5	69.3

**Table 4**

Representative EMP analyses of plagioclase and biotite.

Sample	DP22										DP22			
Texture	Plagioclase relic, rim-core-rim										Symplectic plagioclase			
Point	1	2	3	4	5	6	7	8	9	10	1	2	3	4
SiO <sub>2</sub>	51.5	50.9	49.1	50.1	50.5	51.3	50.9	50.0	50.5	51.0	47.0	46.7	44.2	45.7
Al <sub>2</sub> O <sub>3</sub>	31.6	31.4	30.9	31.9	31.8	30.9	31.6	31.8	31.7	31.3	33.8	34.3	35.8	34.7
FeO	0.06	0.07	0.06	0.09	0.08	0.27	0.04	0.10	0.07	0.05	0.16	0.13	0.15	0.20
CaO	13.5	13.7	14.0	14.1	14.1	13.2	13.9	14.3	13.6	13.7	16.1	16.7	18.7	17.1
Na <sub>2</sub> O	3.55	3.41	3.00	3.11	3.26	3.71	3.43	3.23	3.39	3.42	1.81	1.49	0.45	1.30
K <sub>2</sub> O	0.02	0.03	0.03	0.01	0.01	0.03	0.04	0.02	0.02	0.03	0.01	0.01	0.01	0.01
Total	100.2	99.5	97.1	99.4	99.7	99.5	100.0	99.5	99.3	99.5	98.9	99.3	99.3	99.0
Si	2.33	2.32	2.30	2.29	2.30	2.34	2.31	2.29	2.31	2.32	2.17	2.15	2.05	2.12
Al	1.69	1.69	1.70	1.72	1.71	1.66	1.69	1.71	1.71	1.69	1.84	1.86	1.96	1.89
Fe	0.00	0.00	0.00	0.00	0.00	0.01	0.00	0.00	0.00	0.00	0.01	0.00	0.01	0.01
Ca	0.65	0.67	0.70	0.69	0.69	0.64	0.68	0.70	0.67	0.67	0.80	0.82	0.93	0.85
Na	0.31	0.30	0.27	0.28	0.29	0.33	0.30	0.29	0.30	0.30	0.16	0.13	0.04	0.12
K	0.00	0.00	0.00	0.00	0.00	0.00	0.00	0.00	0.00	0.00	0.00	0.00	0.00	0.00
Total	4.99	4.99	4.99	4.99	4.99	4.99	5.00	5.00	4.99	4.99	4.99	4.98	4.99	4.99
An	67.7	68.8	72.0	71.5	70.5	66.1	69.1	70.8	68.9	68.7	83.0	86.0	95.7	87.9
Ab	32.2	31.1	27.8	28.5	29.5	33.7	30.7	29.1	31.0	31.1	16.9	13.9	4.2	12.1
Sample	DP15										Sample	MS11		
Texture	Plagioclase relic										Biotite	MS8		
Point	1	2	3	1	2	3	4	Point	1	2	3	1	2	3
SiO <sub>2</sub>	50.7	50.1	50.4	45.4	44.8	44.9	44.5	SiO <sub>2</sub>	37.4	36.8	37.2	37.3	37.3	37.7
Al <sub>2</sub> O <sub>3</sub>	31.5	31.7	31.5	35.4	35.6	34.4	34.7	TiO <sub>2</sub>	0.88	0.80	0.79	0.92	0.90	0.87
FeO	0.14	0.22	0.15	0.45	0.55	1.50	1.02	Al <sub>2</sub> O <sub>3</sub>	19.5	19.4	19.2	19.3	19.2	19.0
CaO	13.7	14.3	13.9	18.0	18.3	17.1	17.5	Fe <sub>2</sub> O <sub>3</sub>	1.59	1.52	1.50	1.52	1.57	1.43
Na <sub>2</sub> O	3.42	3.10	3.41	0.80	0.60	0.90	0.75	FeO	8.10	7.73	7.64	7.73	8.01	7.28
K <sub>2</sub> O	0.03	0.03	0.04	0.00	0.01	0.02	0.03	MgO	19.2	19.6	19.0	18.6	18.5	18.9
Total	99.6	99.7	99.5	100.2	100.1	99.4	99.0	Na <sub>2</sub> O	0.79	0.80	0.78	1.73	1.70	1.62
Si	2.31	2.29	2.31	2.09	2.07	2.09	2.07	K <sub>2</sub> O	8.50	8.14	8.58	6.54	6.62	6.53
Al	1.69	1.71	1.70	1.92	1.93	1.89	1.91	F	0.00	0.00	0.00	0.00	0.00	0.00
Fe	0.01	0.01	0.01	0.02	0.02	0.06	0.04	Cl	0.07	0.09	0.09	0.08	0.07	0.10
Ca	0.67	0.70	0.68	0.89	0.90	0.85	0.87	Total	95.9	94.8	94.8	93.6	93.9	93.3
Na	0.30	0.27	0.30	0.07	0.05	0.08	0.07	Si	2.67	2.65	2.69	2.70	2.70	2.73
K	0.00	0.00	0.00	0.00	0.00	0.00	0.00	Ti	0.05	0.04	0.04	0.05	0.05	0.05
Total	4.99	4.99	5.00	4.99	4.99	5.01	5.00	Al	1.64	1.65	1.64	1.65	1.64	1.62
An	68.9	71.8	69.1	92.5	94.4	91.2	92.6	Fe <sup>3+</sup>	0.09	0.08	0.08	0.08	0.09	0.08
Ab	31.0	28.1	30.7	7.5	5.6	8.7	7.2	Fe <sup>2+</sup>	0.48	0.47	0.46	0.47	0.49	0.44
								Mg	2.05	2.11	2.04	2.01	2.00	2.04
								Na	0.11	0.11	0.11	0.24	0.24	0.23
								K	0.78	0.75	0.79	0.61	0.61	0.60
								Total	7.86	7.87	7.86	7.81	7.81	7.79
								Mg#	80.9	81.8	81.5	81.0	80.5	82.2

**Table 5**  
Representative EMP analyses of spinel.

Sample	MS11			MS1					DP1					
Texture	Granular			Granular				Replacing Ol				Granular		
Point	1	2	3	1	2	3	4	1	2	3	4	1	2	3
TiO <sub>2</sub>	0.00	0.03	0.02	0.01	0.00	0.06	0.05	0.04	0.03	0.02	0.05	0.00	0.09	0.06
Al <sub>2</sub> O <sub>3</sub>	62.3	62.0	62.5	62.5	63.3	62.7	62.6	62.3	62.1	62.4	62.7	63.3	63.1	63.3
FeO	27.2	27.6	28.1	23.5	22.7	23.1	23.9	24.5	25.2	24.7	24.0	20.6	20.9	20.5
MnO	0.21	0.23	0.22	0.23	0.22	0.25	0.23	0.26	0.21	0.24	0.23	0.21	0.20	0.16
MgO	11.5	11.7	11.3	14.4	14.2	14.6	14.6	13.6	13.7	13.9	14.3	15.0	14.5	14.4
CaO	0.00	0.00	0.01	0.00	0.01	0.00	0.02	0.01	0.01	0.02	0.01	0.01	0.00	0.00
Cr <sub>2</sub> O <sub>3</sub>	0.01	0.00	0.00	0.01	0.00	0.01	0.02	0.01	0.00	0.02	0.00	0.16	0.20	0.17
Total	101.3	101.5	102.2	100.7	100.6	100.7	101.5	100.8	101.3	101.3	101.4	99.4	99.2	98.7
Ti	0.00	0.00	0.00	0.00	0.00	0.00	0.00	0.00	0.00	0.00	0.00	0.00	0.00	0.00
Al	1.95	1.93	1.95	1.94	1.96	1.94	1.93	1.94	1.93	1.94	1.94	1.96	1.97	1.98
Fe	0.60	0.61	0.62	0.52	0.50	0.51	0.52	0.54	0.56	0.54	0.53	0.45	0.46	0.45
Mn	0.00	0.01	0.01	0.01	0.00	0.01	0.01	0.01	0.00	0.01	0.01	0.00	0.00	0.00
Mg	0.45	0.46	0.45	0.56	0.56	0.57	0.57	0.54	0.54	0.54	0.56	0.59	0.57	0.57
Ca	0.00	0.00	0.00	0.00	0.00	0.00	0.00	0.00	0.00	0.00	0.00	0.00	0.00	0.00
Cr	0.00	0.00	0.00	0.00	0.00	0.00	0.00	0.00	0.00	0.00	0.00	0.00	0.00	0.00
Total	3.01	3.01	3.02	3.03	3.01	3.03	3.03	3.03	3.03	3.03	3.03	3.01	3.01	3.01
Mg#	43.0	43.0	41.8	52.2	52.7	52.9	52.2	49.7	49.2	50.1	51.5	56.4	55.3	55.6
Sample	DP22													
Texture	Symplectitic Sp with Hbl					Granular					Replacing Ol			
Point	1	2	3	4	5	1	2	3	4	5	1	2	3	4
TiO <sub>2</sub>	0.01	0.03	0.04	0.03	0.05	0.09	0.13	0.07	0.07	0.06	0.05	0.03	0.02	0.06
Al <sub>2</sub> O <sub>3</sub>	61.8	62.1	63.2	62.8	63.6	60.9	61.1	60.6	61.9	60.9	61.2	61.4	62.3	60.7
FeO	25.1	24.9	24.6	24.3	23.1	26.4	26.3	26.8	25.7	26.5	27.3	26.6	24.4	26.0
MnO	0.19	0.16	0.15	0.18	0.19	0.16	0.19	0.20	0.19	0.18	0.18	0.19	0.18	0.20
MgO	12.5	12.5	12.9	12.8	13.2	12.4	12.6	12.5	12.7	12.1	11.7	12.0	12.5	12.5
CaO	0.32	0.33	0.13	0.18	0.16	0.01	0.01	0.02	0.00	0.01	0.05	0.02	0.28	0.00
Cr <sub>2</sub> O <sub>3</sub>	0.00	0.00	0.02	0.00	0.00	0.82	0.78	0.97	0.63	0.98	0.47	0.60	0.00	0.75
Total	101.2	101.1	101.5	101.0	100.8	100.9	101.2	101.4	101.4	100.8	101.2	101.0	100.7	100.4
Ti	0.00	0.00	0.00	0.00	0.00	0.00	0.00	0.00	0.00	0.00	0.00	0.00	0.00	0.00
Al	1.92	1.93	1.95	1.95	1.96	1.92	1.92	1.91	1.93	1.92	1.93	1.93	1.94	1.92
Fe	0.55	0.55	0.54	0.54	0.51	0.59	0.58	0.60	0.57	0.59	0.61	0.59	0.54	0.58
Mn	0.00	0.00	0.00	0.00	0.00	0.00	0.00	0.00	0.00	0.00	0.00	0.00	0.00	0.00
Mg	0.49	0.49	0.50	0.50	0.51	0.49	0.50	0.50	0.50	0.48	0.47	0.48	0.49	0.50
Ca	0.01	0.01	0.00	0.01	0.00	0.00	0.00	0.00	0.00	0.00	0.00	0.00	0.01	0.00
Cr	0.00	0.00	0.00	0.00	0.00	0.02	0.02	0.02	0.01	0.02	0.01	0.01	0.00	0.02
Total	2.98	2.98	3.00	3.00	2.99	3.03	3.03	3.03	3.02	3.02	3.03	3.02	2.98	3.02
Mg#	47.1	47.3	48.2	48.5	50.4	45.6	46.1	45.3	46.8	44.9	43.4	44.6	47.8	46.2

Compositions of fibrous hornblende at the outer edge of the olivine and plagioclase corona vary greatly from magnesiosadanagaite to pargasite, with lower Si, higher Al and variable Ca contents. In samples with igneous relics, the prismatic hornblende may be pargasite or magnesiohornblende, with variable, but overall higher Si and Ca and lower Al contents. The compositional variation of hornblende in samples that underwent incomplete metamorphism (with igneous relics) may be directly related to the precursor minerals they replaced.

#### 5.1.7. Biotite

Biotite from the mylonite of the Mianhuadi mafic complex is relatively homogeneous in composition with Mg# ranging from 80.5 to 82.2; there are limited variations in Na<sub>2</sub>O and K<sub>2</sub>O contents (Table 4). It has high Al<sub>2</sub>O<sub>3</sub> contents (18.8–19.5 wt.%) and low SiO<sub>2</sub> contents (36.8–38.4 wt.%). The F and Cl contents are negligible, but overall Cl is slightly higher than F, which is commonly below the detection limit.

#### 5.2. Ar-Ar age of biotite

Foliated biotite from one mylonite sample (MS11) of the Mianhuadi mafic complex has a plateau <sup>40</sup>Ar/<sup>39</sup>Ar age of 34.3 ± 0.4 Ma and a consistent inverse isochron age of 34.1 ± 0.6 Ma (Fig. 7, Table 7).

## 6. Discussion

### 6.1. The protolith of the Mianhuadi mafic complex

The relict textures and pre-metamorphic minerals of the Mianhuadi mafic complex indicate that the protolith was comparable to Fe-Ti oxide-bearing layered mafic-ultramafic intrusions, such as the Panzhihua, Hongge and Baima intrusions, in the Panzhihua-Xichang area of the ELIP (e.g. Pang et al., 2008, 2009; Bai et al., 2012; Song et al., 2013; Wang and Zhou, 2013; Liu et al., 2014a,b). Zircon U-Pb ages (259.6 ± 0.8 Ma) and high Th/U ratios (> 0.3) reported by Zhou et al. (2013) also suggest that the protolith of the Mianhuadi mafic complex was magmatic in origin and that the zircon age represent the emplacement age of this mafic intrusion. Accordingly, the protolith of the Mianhuadi mafic complex is interpreted to be part of the ELIP, which is recognized to be derived from a starting mantle plume that interacted with the lithospheric mantle at the time of the Permian-Triassic boundary (Chung and Jahn, 1995; Xu et al., 2001).

In addition to layered intrusions, the ELIP is composed of flood basalts that cover a large area in SW China and northern Vietnam (e.g. Liu et al., 2017 and references therein). The southern part of the ELIP might have been displaced considerably southeastwards along the

**Table 6**  
Representative EMP analyses of hornblende.

Texture	Undeformed prismatic Hbl										Hbl + Pl symplectite										
	MS1						DP21					DP22					DP15				
Point	1	2	3	4	5	6	1	2	3	4	5	1	2	3	4	1	2	3	4	5	
SiO <sub>2</sub>	45.3	45.4	45.6	46.3	44.9	43.3	47.0	43.6	44.4	52.0	50.8	42.7	42.3	42.4	41.6	41.9	42.0	41.3	40.5	40.9	
TiO <sub>2</sub>	0.49	0.56	0.54	0.56	0.38	0.40	0.41	0.70	0.71	0.29	0.36	0.15	0.16	0.31	0.15	0.10	0.06	0.12	0.05	0.07	
Al <sub>2</sub> O <sub>3</sub>	12.8	12.9	13.1	12.3	11.8	11.5	11.9	14.5	14.0	6.5	7.9	15.8	16.7	16.5	16.8	16.9	16.6	17.5	18.2	18.1	
Fe <sub>2</sub> O <sub>3</sub>	3.14	3.76	3.99	3.44	3.61	7.04	4.51	3.06	3.14	2.78	2.72	4.79	3.55	3.92	3.50	2.65	2.99	2.94	3.77	4.28	
FeO	5.39	4.80	5.15	4.89	4.91	1.75	4.50	6.54	6.71	4.58	5.04	9.47	9.81	9.51	9.60	11.2	11.0	10.0	9.22	9.18	
MnO	0.16	0.14	0.16	0.16	0.16	0.14	0.17	0.09	0.12	0.11	0.10	0.21	0.21	0.24	0.24	0.14	0.10	0.10	0.09	0.10	
MgO	15.5	15.7	15.5	16.0	15.7	16.5	16.3	14.4	14.4	18.6	17.6	11.9	11.4	11.6	11.5	11.2	11.2	11.4	11.4	11.5	
CaO	12.2	11.9	11.8	12.1	12.8	11.0	11.6	12.3	12.3	12.2	11.9	11.1	11.2	11.1	11.2	11.7	11.4	11.5	11.4	11.1	
Na <sub>2</sub> O	1.63	1.66	1.70	1.48	1.50	1.20	1.57	1.99	1.80	0.82	1.00	2.36	2.38	2.37	2.53	2.71	2.59	2.68	2.71	2.77	
K <sub>2</sub> O	0.20	0.18	0.21	0.16	0.15	0.15	0.10	0.13	0.12	0.03	0.04	0.19	0.21	0.21	0.23	0.32	0.25	0.28	0.34	0.29	
F	0.00	0.00	0.00	0.00	0.00	0.00	0.00	0.00	0.00	0.00	0.00	0.00	0.00	0.00	0.00	0.00	0.00	0.00	0.00	0.00	
Cl	0.14	0.13	0.13	0.10	0.13	0.09	0.12	0.22	0.20	0.04	0.07	0.06	0.07	0.07	0.06	0.04	0.05	0.03	0.01	0.01	
Total	96.8	97.0	97.8	97.3	95.9	93.0	98.1	97.2	97.7	97.9	97.6	98.6	97.9	98.2	97.3	98.7	98.1	97.8	97.8	98.4	
Si	6.52	6.50	6.49	6.59	6.53	6.44	6.63	6.29	6.37	7.27	7.14	6.18	6.16	6.14	6.10	6.09	6.13	6.03	5.92	5.93	
Ti	0.05	0.06	0.06	0.06	0.04	0.04	0.04	0.08	0.08	0.03	0.04	0.02	0.02	0.03	0.02	0.01	0.01	0.01	0.01	0.01	
Al	2.17	2.18	2.20	2.06	2.02	2.01	1.98	2.46	2.37	1.07	1.32	2.69	2.86	2.83	2.90	2.90	2.85	3.01	3.14	3.10	
Fe <sup>3+</sup>	0.34	0.41	0.43	0.37	0.40	0.79	0.48	0.33	0.34	0.29	0.29	0.52	0.39	0.43	0.39	0.29	0.33	0.32	0.42	0.47	
Fe <sup>2+</sup>	0.65	0.57	0.61	0.58	0.60	0.22	0.53	0.79	0.80	0.54	0.59	1.15	1.19	1.15	1.18	1.36	1.34	1.23	1.13	1.11	
Mn	0.02	0.02	0.02	0.02	0.02	0.02	0.02	0.01	0.01	0.01	0.01	0.03	0.03	0.03	0.03	0.02	0.01	0.01	0.01	0.01	
Mg	3.31	3.35	3.29	3.39	3.40	3.66	3.43	3.09	3.08	3.87	3.70	2.56	2.47	2.51	2.50	2.42	2.43	2.48	2.49	2.49	
Ca	1.88	1.82	1.79	1.84	1.99	1.75	1.76	1.90	1.88	1.82	1.80	1.72	1.74	1.72	1.75	1.81	1.79	1.79	1.79	1.73	
Na	0.45	0.46	0.47	0.41	0.42	0.35	0.43	0.56	0.50	0.22	0.27	0.66	0.67	0.67	0.72	0.76	0.73	0.76	0.77	0.78	
K	0.04	0.03	0.04	0.03	0.03	0.03	0.02	0.02	0.02	0.01	0.01	0.04	0.04	0.04	0.04	0.06	0.05	0.05	0.06	0.05	
Total	15.5	15.5	15.5	15.5	15.4	15.6	15.5	15.6	15.6	15.2	15.3	15.7	15.7	15.7	15.8	15.8	15.8	15.8	15.9	15.9	
Texture	Radial Hbl						Deformed prismatic Hbl						Hbl + Sp symplectite						DP22		
Sample	DP15						MS11						DP22						DP22		
Point	1	2	3	4	5	6	1	2	3	4	5	1	2	3	4	5	1	2	3	4	5
SiO <sub>2</sub>	34.2	39.3	40.0	37.5	35.7	40.3	41.9	42.4	42.3	41.8	41.4	43.1	43.3	42.0	43.3	43.1	43.3	42.0	43.3	43.1	
TiO <sub>2</sub>	0.01	0.07	0.00	0.01	0.69	0.72	0.44	0.61	0.57	0.52	0.64	0.28	0.27	0.27	0.30	0.28	0.27	0.27	0.27	0.28	
Al <sub>2</sub> O <sub>3</sub>	25.5	19.1	17.0	22.3	20.5	16.1	17.2	16.6	16.6	17.0	17.3	15.0	15.2	16.0	15.2	15.1	16.0	15.2	15.1	15.1	
Fe <sub>2</sub> O <sub>3</sub>	9.05	9.09	5.02	8.39	10.14	5.51	5.00	3.94	4.50	4.54	3.61	6.22	4.82	5.28	4.72	4.59	4.72	4.59	4.72	4.59	
FeO	8.51	4.20	6.74	5.70	4.51	6.19	6.64	7.65	7.04	6.61	8.06	4.10	5.35	5.09	5.25	5.44	5.25	5.44	5.25	5.44	
MnO	0.13	0.14	0.13	0.09	0.10	0.14	0.14	0.15	0.14	0.14	0.14	0.20	0.16	0.16	0.14	0.14	0.16	0.16	0.14	0.14	
MgO	11.3	13.9	12.8	12.8	13.1	13.4	13.3	13.3	13.4	13.5	12.6	15.3	15.0	14.5	15.1	15.0	14.5	15.1	15.0	15.0	
CaO	9.19	10.7	11.6	10.6	9.88	11.5	11.7	11.9	11.7	11.7	11.8	11.2	11.3	11.3	11.3	11.1	11.3	11.1	11.3	11.1	
Na <sub>2</sub> O	2.32	2.51	2.86	2.44	2.31	2.81	2.38	2.33	2.33	2.46	2.35	2.62	2.75	2.75	2.72	2.86	2.75	2.75	2.72	2.86	
K <sub>2</sub> O	0.18	0.14	0.22	0.19	0.09	0.12	0.44	0.55	0.47	0.49	0.60	0.16	0.21	0.27	0.22	0.19	0.21	0.27	0.22	0.19	
F	0.00	–	–	–	–	–	0.00	0.00	0.00	0.00	0.00	0.00	0.00	0.00	0.00	0.00	0.00	0.00	0.00	0.00	
Cl	0.00	0.02	0.01	0.01	0.03	0.02	0.17	0.10	0.10	0.13	0.11	0.08	0.07	0.06	0.06	0.06	0.06	0.06	0.06	0.03	
Total	100.3	99.1	96.3	100.1	97.1	96.8	99.1	99.4	99.0	98.8	98.5	98.1	98.3	97.6	98.2	97.7	97.7	97.7	97.7	97.7	
Si	4.92	5.61	5.90	5.34	5.25	5.91	5.98	6.05	6.05	5.99	5.97	6.15	6.18	6.05	6.19	6.18	6.15	6.18	6.18	6.18	
Ti	0.00	0.01	0.00	0.00	0.08	0.08	0.05	0.07	0.06	0.06	0.07	0.03	0.03	0.03	0.03	0.03	0.03	0.03	0.03	0.03	
Al	4.32	3.22	2.95	3.74	3.56	2.79	2.90	2.80	2.79	2.87	2.95	2.52	2.56	2.73	2.56	2.56	2.56	2.56	2.56	2.56	
Fe <sup>3+</sup>	0.98	0.98	0.56	0.90	1.12	0.61	0.54	0.42	0.48	0.49	0.39	0.67	0.52	0.57	0.51	0.50	0.51	0.50	0.51	0.50	
Fe <sup>2+</sup>	1.03	0.50	0.83	0.68	0.56	0.76	0.79	0.91	0.84	0.79	0.97	0.49	0.64	0.61	0.63	0.65	0.62	0.62	0.62	0.65	
Mn	0.02	0.02	0.02	0.01	0.01	0.02	0.02	0.02	0.02	0.02	0.02	0.02	0.02	0.02	0.02	0.02	0.02	0.02	0.02	0.02	
Mg	2.42	2.95	2.82	2.71	2.87	2.92	2.83	2.82	2.86	2.89	2.71	3.25	3.19	3.11	3.20	3.20	3.20	3.20	3.20	3.20	
Ca	1.42	1.64	1.84	1.62	1.56	1.81	1.79	1.81	1.79	1.79	1.82	1.71	1.72	1.74	1.72	1.74	1.72	1.74	1.72	1.74	
Na	0.65	0.70	0.82	0.67	0.66	0.80	0.66	0.64	0.65	0.68	0.66	0.73	0.76	0.77	0.75	0.76	0.77	0.75	0.76	0.78	
K	0.03	0.03	0.04	0.04	0.02	0.02	0.08	0.10	0.09	0.09	0.11	0.03	0.04	0.05	0.04	0.05	0.04	0.05	0.04	0.03	
Total	16.1	16.0	16.0	16.0	16.1	15.9	15.81	15.79	15.79	15.83	15.8	15.8	15.9	15.8	15.9	15.8	15.9	15.8	15.9	15.8	

ASRR shear zone, as suggested by two well-correlated markers, namely picritic lavas in the Late Permian flood basalt successions and mafic rocks of the late Paleogene alkaline rock suite, which underwent a consistent left-lateral offset of ~500 km (Chung et al., 1997). In this sense, Permian flood basalts in the Song Da belt and the Ban Phu Ni-Cu deposit of Vietnam, and flood basalts and the Baimazhai Ni-Cu deposit in Jinping of Yunnan represent a southern extension of the Permian ELIP (Gong, 1988; Wang et al., 2007).

So far, most high-grade metamorphic rocks in the ASRR shear zone were reported to have an old pre-Cambrian protolith (> 500 Ma) of the

basement complexes (e.g. Lin et al., 2012; Liu et al., 2013) and the previous thermal event(s) were commonly obscured by the latest deformation associated with the Tertiary sinistral shearing. Unlike the other metamorphic basement rocks, the Mianhuadi mafic complex with a Late Permian magmatic protolith, is thus much younger and records simpler metamorphic events that were not completely overprinted by later mylonitization. The identification of the Permian protolith clearly indicates that the metamorphic massifs in the ASRR shear zone are not necessarily parts of the old Proterozoic basement.

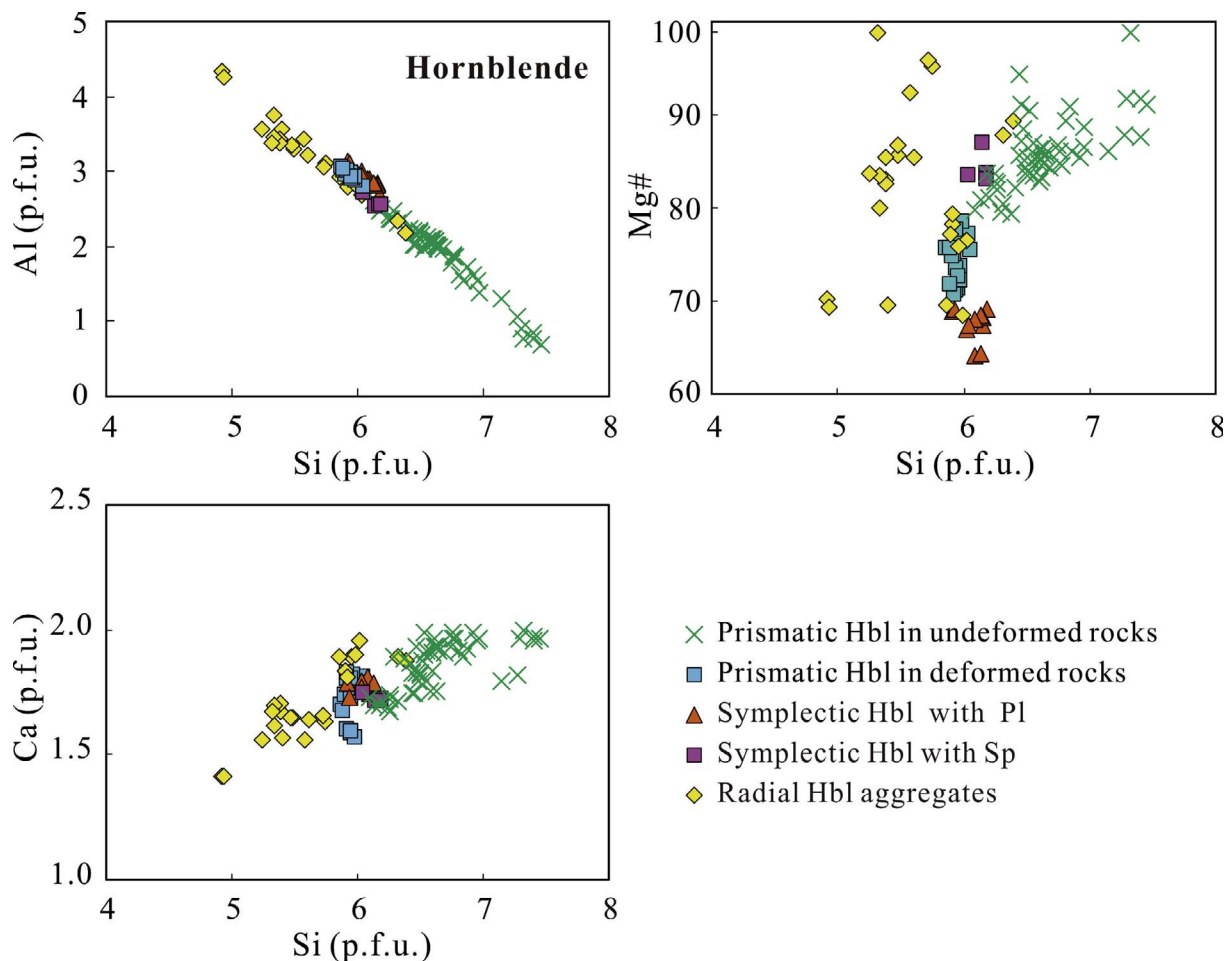


Fig. 6. Plots of Al (p.f.u.) vs. Si (p.f.u.), Mg# vs. Si (p.f.u.) and Ca (p.f.u.) vs. Si (p.f.u.) for hornblende in the Mianhuadi mafic complex.

## 6.2. P-T estimates

The Mianhuadi mafic complex was originally dominated by an anhydrous mineral assemblage of olivine + clinopyroxene + plagioclase + magnetite + ilmenite + spinel  $\pm$  apatite. Hornblende + spinel symplectites have been reported in metamorphosed mafic rocks, as a result of the reaction between olivine and plagioclase (Ashworth, 1986; Cruciani et al., 2008; Gallien et al., 2012). Hornblende + anorthite symplectites have been reported in metamorphosed mafic rocks replacing garnet (Smithies and Bagas, 1997; Zhao et al., 2000, 2001, 2003; Zhang et al., 2010, 2014) or omphacite (Okay et al., 1989). Both types of symplectites were identified as decompressional mineral assemblages (Clarke and Powell, 1991; Zhao et al., 2001). Our study of the Mianhuadi mafic complex, which hosts Fe-Ti oxide ores, has revealed that metamorphic reactions involving silicate-bearing Fe-Ti oxide ores do not differ much from those affecting mafic rocks, such as gabbro and dolerite. Therefore, metamorphosed Fe-Ti oxide-bearing gabbros and Fe-Ti oxide ores, like other gabbroic rocks, can be used to deduce metamorphic processes.

The peak-stage temperature conditions calculated from the garnet rim and clinopyroxene of the granulites from the Mianhuadi mafic complex vary from 657 to 693 °C, using an estimated pressure of 8 kbar, whereas the orthopyroxene thermometer (Brey and Köhler, 1990) indicates a slightly higher peak metamorphic temperature of 722 °C (Table 8). The peak pressure conditions calculated from the garnet-orthopyroxene and garnet-orthopyroxene-clinopyroxene-plagioclase assemblages indicate pressures of 9 and 7 kbar, respectively, using an estimated temperature of 687 °C. Therefore the peak P-T conditions were best estimated to be 7–9 kbar and 657–722 °C.

The retrograde temperatures estimated by the garnet-amphibole

assemblage (Graham and Powell, 1984; Ravna, 2000) range from 649 to 676 °C. Using an average equilibrium temperature of 663 °C, the retrograde pressures estimated by the garnet-amphibole-plagioclase thermobarometer (Kohn and Spear, 1989, 1990) are 5–6 kbar. Considering the roughly comparable metamorphic temperatures between peak and retrograde stages, the Mianhuadi mafic complex likely experienced a near-isothermal decompression following the granulite-facies peak metamorphism, suggesting rapid exhumation (e.g. Zhao et al., 2000, 2001; Zhang et al., 2010, 2014).

## 6.3. Granulite facies metamorphism on the Mianhuadi mafic complex: when and how?

The emplacement of the protolith of the Mianhuadi mafic complex at  $\sim$  260 Ma suggests that the metamorphic event(s) must have taken place after the Late Permian. There have been two metamorphic events since the Late Permian in SE Asia. The metamorphic basement of central Vietnam, away from the ASRR shear zone, experienced an episode of high-temperature granulite-facies metamorphism in the Late Permian-Early Triassic (260–240 Ma) followed by a rapid exhumation at  $243 \pm 5$  Ma (Carter et al., 2001). Inclusions in zircon from the Diancang Shan-Ailao Shan metamorphic massifs also imply an Early-Middle Triassic (249–230 Ma) high-pressure metamorphic event (650–720 °C,  $\sim 14$  kb) along the ASRR shear zone (Liu et al., 2013). This Late Permian-Middle Triassic metamorphism is considered to have been due to accretion of the Sibumasu to the Indochina-South China (Metcalfe, 1995; Carter et al., 2001). The second metamorphic event occurred in the Tertiary and reached peak pressure-temperature conditions of 720–805 °C and 8.0–9.6 kbar between 44 and 34 Ma (Liu

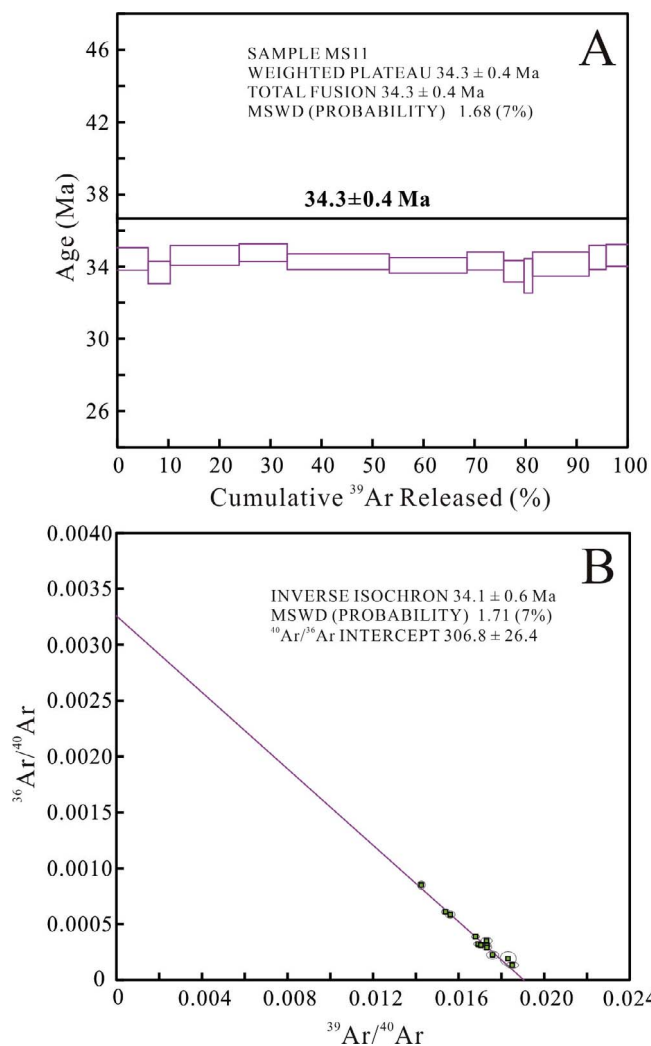


**Fig. 7.**  $^{40}\text{Ar}/^{39}\text{Ar}$  data for biotite from mylonites of the Mianhuadi mafic complex. A.  $^{40}\text{Ar}/^{39}\text{Ar}$  step-heating spectra (12 steps) of biotite from sample MS11 and a plateau age of  $34.3 \pm 0.4$  Ma was obtained. B. Inverse isochron, including 12 steps of the analysis, obtained from the step-heating experiment on the same biotite.

et al., 2013; Palin et al., 2013), after which exhumation occurred almost immediately (Palin et al., 2013). The causes for the Tertiary metamorphism remain a matter of debate. Earlier studies proposed that high temperatures in the shear zone resulted from shear heating by ascent of magmas and/or fluids (Leloup and Kienast, 1993; Leloup et al., 1995). An alternative view is that the high-grade metamorphism along the ASRR shear zone was due to the India-Asia collision (Lin et al., 2012; Liu et al., 2013) and the left-lateral kinematic indicators are low-

**Table 8**

Calculated P-T conditions of peak and retrograde stage metamorphism of the Mianhuadi mafic complex.

Stage	Method	P condition	T condition	Reference
Peak stage	Grt-Cpx	8 <sup>a</sup>	657	Krogh (1988)
			693	Ellis and Green (1979)
	Opx		675	Powell (1985)
			722	Brey and Köhler (1990)
	Grt-Opx	9	687 <sup>a</sup>	Harley (1984)
	Grt-Opx-Cpx-Pl	7	687 <sup>a</sup>	Paria et al. (1988)
	Grt-Amp		676	Graham and Powell (1984)
			649	Ravna (2000)
	Grt-Amp-Pl	6	663 <sup>a</sup>	Kohn and Spear (1990)
			663 <sup>a</sup>	Kohn and Spear (1989)
Grt-garnet, Cpx-clinopyroxene. Opx-orthopyroxene, Pl-plagioclase, Amp-amphibole.				

<sup>a</sup> Estimated pressure (P) or temperature (T) used in the calculation of T or P, respectively.

temperature fabrics. Thus the ASRR strike-slip shear was considered to be only an upper and middle crust phenomenon (Jolivet et al., 2001; Searle, 2006). The Late Permian-Middle Triassic metamorphism was less frequently documented in the ASRR shear zone compared with the Tertiary metamorphism.

The Mianhuadi mafic complex is located between the Ailaoshan and DNCV massifs. A large majority of Late Permian-Early Triassic zircon from the Ailaoshan and DNCV massifs displayed magmatic internal structures, sometimes with a narrow metamorphic rim formed during Eocene (Searle et al., 2010; Lin et al., 2012). The Late Permian-Early Triassic metamorphic zircon was found locally and commonly formed under high pressures (Liu et al., 2013). The Mianhuadi mafic complex does not have textures/mineral assemblages related to high-pressure metamorphism. Moreover, considering the Late Permian-Early Triassic metamorphism was not a widespread event within the ASRR shear zone, we prefer that the metamorphism of the Mianhuadi mafic complex occurred in the Tertiary before the Late Eocene deformation.

The widely preserved mineral relics and symplectites in the Mianhuadi mafic complex indicate that the high-grade metamorphic conditions did not last long. This is consistent with the rapid exhumation after peak stage metamorphism in the Eocene (Palin et al., 2013). Peak stage metamorphic conditions calculated using P-T pseudosection from previous studies indicated that the granulite-facies conditions ( $720\text{--}805^\circ\text{C}$  and  $8.0\text{--}9.6\text{ kbar}$ ) have been reached during Tertiary metamorphism between  $\sim 44$  and  $34\text{ Ma}$ , although typical granulite-facies mineral assemblage was not found (Liu et al., 2013; Palin et al., 2013). The occurrence of orthopyroxene in the Mianhuadi mafic

**Table 7**

$^{40}\text{Ar}/^{39}\text{Ar}$  analytical data of biotite from mylonites of the Mianhuadi mafic complex.

Laser power (%)	$^{40}\text{Ar}/^{39}\text{Ar}$	$^{37}\text{Ar}/^{39}\text{Ar}$	$^{36}\text{Ar}/^{39}\text{Ar}$	$^{40}\text{Ar}^*/^{39}\text{Ar}_k$	$^{40}\text{Ar}^*/(\%)$	$^{39}\text{Ar}_k (\%)$	Age (Ma)	$\pm 2\text{ s (Ma)}$
1.50 W	64.040	0.00429	0.03755	52.944	82.67	6.05	34.4	$\pm 0.6$
1.60 W	57.781	0.00576	0.02030	51.784	89.62	4.32	33.7	$\pm 0.6$
1.60 W	64.966	0.00196	0.03967	53.244	81.96	13.49	34.6	$\pm 0.5$
1.70 W	59.105	0.00275	0.01905	53.476	90.48	9.42	34.8	$\pm 0.5$
1.70 W	59.557	0.00130	0.02318	52.709	88.50	20.02	34.3	$\pm 0.4$
1.80 W	57.713	0.00171	0.01800	52.395	90.79	15.23	34.1	$\pm 0.4$
1.80 W	57.713	0.00375	0.01677	52.759	91.42	7.17	34.3	$\pm 0.5$
1.90 W	54.026	0.00669	0.00726	51.882	96.03	3.98	33.7	$\pm 0.6$
2.00 W	54.597	0.01584	0.01050	51.494	94.32	1.67	33.5	$\pm 0.9$
2.10 W	70.133	0.00241	0.05966	52.505	74.86	11.06	34.1	$\pm 0.7$
2.20 W	56.853	0.00834	0.01277	53.080	93.36	3.34	34.5	$\pm 0.7$
2.30 W	58.671	0.00628	0.01834	53.252	90.76	4.24	34.6	$\pm 0.6$

complex, from a mineral assemblage perspective, proves that the metamorphic event associated with the ASRR shear zone reached granulite facies conditions (Green and Ringwood, 1967). Coronas around olivine and plagioclase also indicate their formation under typical medium- to high-pressure, amphibolite-granulite facies metamorphic terrains (e.g. Gallien et al., 2012; Gardner and Robins, 1974). Our study thus provided robust petrographic evidence that granulite facies was reached during Tertiary, possibly Eocene, metamorphism along the ASRR shear zone.

The Eocene metamorphism within the ASRR shear zone could be induced by regional heating prior to shearing. The required heat source/flow could be related to upwelling of the asthenosphere induced by delamination of the thickened continental lithosphere during ~40–30 Ma (Chung et al., 1997; Lu et al., 2013). Partial melting of thickened lower crust and lithospheric mantle at this period also produced a 2000 km long Eocene potassic magmatic belt across the Qiangtang Terrane and Yangtze Block (Lu et al., 2013). This alkaline magmatism intrudes within, close to or away from the ASRR shear zone and has no genetic correlation with initiation of the shearing (Chung et al., 2008). Among them, the Jinping (FanSiPan) alkali granite, one of the largest alkaline igneous bodies south of the Mianhuadi mafic complex, was intruded at  $35.0 \pm 0.3$  Ma (Zhang and Schärer, 1999). If the Eocene metamorphism occurred coeval with the alkaline magmatism, the sinistral shearing and exhumation of the ASRR shear zone was initiated shortly after. This may explain the widely preserved relics and differential metamorphism of the Mianhuadi mafic complex.

Combined with previous studies, we propose that the mechanism of the Eocene metamorphism started with an overthickened crust and continental lithospheric mantle, as indicated by potassic adakite-like rocks (Lu et al., 2013), along the boundary between the Simao and Yangtze blocks induced by the India-Asia collision at around 55–40 Ma (Fig. 8a). Then, removal of the overthickened continental lithospheric mantle led to asthenosphere upwelling at 40–35 Ma, which induced melting of the lower crust and continental lithospheric mantle and produced terrains of granulite-facies and amphibolite-facies P-T conditions. This period is also accompanied by regional extension and emplacement of highly potassic mafic magmas (Fig. 8b; Chung et al., 1997). Finally, rapid exhumation following the removal of the continental lithospheric mantle occurred and the ductile shearing was developed to accommodate the eastward extrusion of Indochina probably with the aid of hydrous fluids released partly from exhumation of the metamorphic rocks (Fig. 8c; Cao et al., 2017).

#### 6.4. Initial timing of left-lateral ductile deformation along the ASRR shear zone

The relationship between the metamorphism and shearing along the ASRR shear zone has been a matter of considerable debate and no consensus has reached. Early studies concluded that the metamorphic and igneous rocks formed as a result of shear heating contemporaneous with Tertiary left-lateral shearing along the ASRR shear zone (Tapponnier et al., 1982, 1990; Leloup et al., 1993, 2001). Later studies suggested that high-grade metamorphism and magmatic intrusion occurred before shearing (Chung et al., 1997; Searle, 2006; Searle et al., 2010; Liu et al., 2013). Syn-kinematic mylonites are interpreted to have developed under regional greenschist facies conditions (Yeh et al., 2014). In our study, some of the amphibolite-granulite facies metamorphic rocks from the Mianhuadi mafic complex preserve delicate symplectitic textures and do not show evidence of deformation and foliation. Other rocks are characterized by mylonitic foliations of hornblende and biotite. These rocks thus provide convincing petrographic evidence that mylonitic deformation associated with the shearing occurred after the amphibolite-granulite facies metamorphism and destroyed the delicate metamorphic textures.

The issue of the initial timing of the ductile shearing along the ASRR shear zone is complex and has been difficult to resolve despite large

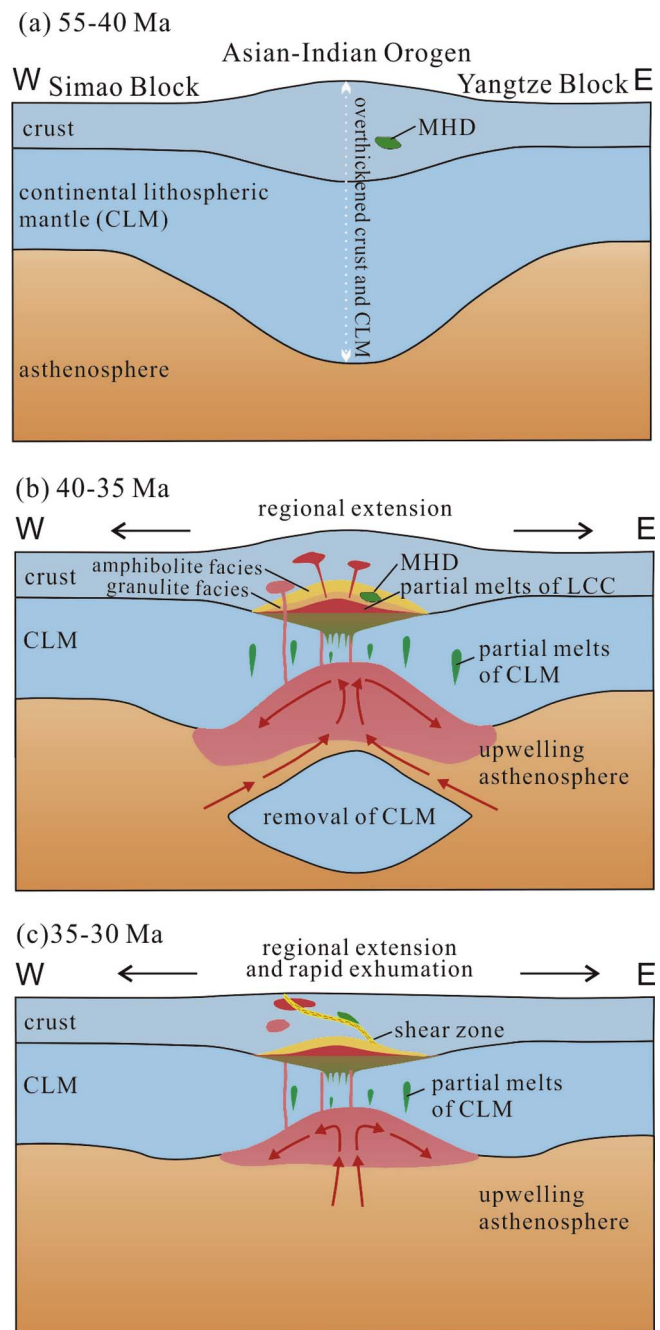


**Fig. 8.** Schematic illustration of the mechanism for Eocene metamorphism and shearing along the ASRR shear zone in the western Yangtze Block. (a) The Eocene metamorphism started with an overthickened crust and continental lithospheric mantle along the boundary between the Simao Block and Yangtze Block induced by India-Asia collision around 55–40 Ma. (b) Removal of the overthickened continental lithospheric mantle led to asthenosphere upwelling at 40–35 Ma, which induced melting of the lower crust and continental lithospheric mantle and produced terrains of granulite-facies and amphibolite-facies P-T conditions. (c) Rapid exhumation following removal of the continental lithospheric mantle occurred from ~35 Ma and the ductile shearing was developed to accommodate the eastward extrusion of Indochina.

numbers of age determinations. A significant clustering of K-Ar ages for clay minerals from gouge within the normal faults of the ASRR shear zone at 20–25 Ma (Harrison et al., 1992) and U-Pb ages of 22–27 Ma for small leucogranitic bodies (Schärer et al., 1994) indicate that there were intense shear movements between the late Oligocene to early Miocene. Searle (2006) proposed that the left-lateral shearing started after 21 Ma and the fault was purely a crustal structure. But he later revised his interpretation of the initial timing of the ductile shearing in

the ASRR to after 31.9 Ma by combining all the available U-Th-Pb age data (Searle et al., 2010). However, Leloup et al. (2001) and Liu et al. (2013) suggested that the left-lateral strike-slip movement likely started prior to 32 Ma and continued until ~16–14 Ma. Gilley et al. (2003) dated monazite inclusions in syntectonic garnets using the Th-Pb method and concluded that the left-lateral shearing within the ASRR shear zone occurred between 34 and 21 Ma. Finally Cao et al. (2011) provided a detailed history of the shearing which is interpreted to have initiated at ~31 Ma, culminated between 27 and 21 Ma and slowed down at ~20 Ma.

Our Ar-Ar ages of foliated biotite from the mylonite of the Mianhuadi mafic complex show that the left-lateral strike-slip movement started at or prior to  $34.3 \pm 0.4$  Ma, clearly demonstrating that the ASRR shear zone was active before the Oligocene, earlier than previously thought. The coeval delamination of thickened continental lithosphere and upwelling of asthenosphere deduced from the 2000 km long Eocene potassic magmatic belt (Chung et al., 1997; Lu et al., 2013) possibly contributed to the initiation of the sinistral ductile shearing, which accommodated the northward coupling of India to Asia.

## 7. Conclusions

Petrography and mineralogy of the granulite and mylonite from the Mianhuadi mafic complex and Ar-Ar dates of foliated biotite from mylonites indicate the following conclusions:

1. The Mianhuadi mafic complex has a protolith of Permian oxide-bearing mafic-ultramafic intrusions and underwent granulite facies metamorphism with peak P-T conditions of 657–722 °C and 7–9 kbar, followed by retrograde metamorphism at P-T conditions of 649–676 °C and 5–6 kbar. Near-isothermal decompression following the peak metamorphism indicates rapid exhumation.
2. Granulite-facies metamorphism of the Mianhuadi mafic complex likely occurred in the Eocene, prior to the ductile sinistral shearing of the ASRR shear zone.
3. Eocene granulite-facies metamorphism of the ASRR shear zone could have resulted from asthenosphere upwelling, which also produced numerous alkaline intrusions that were emplaced both within and outside the ASRR shear zone.

## Acknowledgements

This paper is dedicated to Prof. Bor-ming Jahn who passed away in December 2016. We are grateful to Dr. Xin-Fu Zhao for his field work assistance. We would like to thank Drs. Danping Yan, Hafiz Ur Rehman, Changqing Yin and Meiling Wu for helpful discussions during preparation of the manuscript. Dr. A.E. Williams-Jones and two anonymous reviewers are thanked for improving an earlier version of the manuscript. This research was supported by National Science Foundation of China (Grant No. 41325006 and 41503010), China Postdoctoral Science Foundation (2015M570145) and CRCG grants from HKU.

## References

- Allen, C.R., Gillespie, A., Yuan, H., Sieh, K.E., Buchun, Z., Chengnan, Z., 1984. Red River and associated faults, Yunnan Province, China: quaternary geology, slip rates, and seismic hazard. *Geol. Soc. Am. Bull.* 95, 686–700.
- Ashworth, J., 1986. The role of magmatic reaction, diffusion, and annealing in the evolution of coronitic microstructure in troctolitic gabbro from Risør, Norway: a discussion. *Mineral. Mag.* 50, 469–473.
- Bai, Z.-J., Zhong, H., Naldrett, A.J., Zhu, W.-G., Xu, G.-W., 2012. Whole-rock and mineral composition constraints on the genesis of the giant Hongge Fe-Ti-V oxide deposit in the Emeishan Large Igneous Province, Southwest China. *Econ. Geol.* 107, 507–524.
- Brey, G., Köhler, T., 1990. Geothermobarometry in four-phase herzolites II. New thermobarometers, and practical assessment of existing thermobarometers. *J. Petrol.* 31, 1353–1378.
- Cao, S., Liu, J., Leiss, B., Neubauer, F., Genser, J., Zhao, C., 2011. Oligo-Miocene shearing along the Ailao Shan-Red River shear zone: constraints from structural analysis and zircon U/Pb geochronology of magmatic rocks in the Diancang Shan massif, SE Tibet, China. *Gondwana Res.* 19, 975–993.
- Cao, S., Neubauer, F., Liu, J., Bernroder, M., Cheng, X., Li, J., Yu, Z., Genser, J., 2017. Rheological weakening of high-grade mylonites during low-temperature retrogression: the exhumed continental Ailao Shan-Red River fault zone, SE Asia. *J. Asian Earth Sci.* 139, 40–60.
- Carter, A., Roques, D., Bristow, C., Kinny, P., 2001. Understanding Mesozoic accretion in Southeast Asia: significance of Triassic thermotectonism (Indosinian orogeny) in Vietnam. *Geology* 29, 211–214.
- Chung, S.-L., Jahn, B.-M., 1995. Plume-lithosphere interaction in generation of the Emeishan flood basalts at the Permian-Triassic boundary. *Geology* 23, 889–892.
- Chung, S.-L., Lee, T.-Y., Lo, C.-H., Wang, P.-L., Chen, C.-Y., Yen, N.T., Hoa, T.T., Genyao, W., 1997. Intraplate extension prior to continental extrusion along the Ailao Shan-Red River shear zone. *Geology* 25, 311–314.
- Chung, S.L., Searle, M.P., Yeh, M.W., 2008. The age of the potassic alkaline igneous rocks along the Ailao Shan-Red River shear zone: implications for the onset age of left-lateral shearing: A discussion. *J. Geol.* 116, 201–204.
- Clarke, G., Powell, R., 1991. Decompressive coronas and symplectites in granulites of the Musgrave Complex, central Australia. *J. Metamorph. Geol.* 9, 441–450.
- Cong, B., 1988. Formation and Evolution of the Panxi Paleorift. Science Press, Beijing.
- Cruciani, G., Franceschelli, M., Groppo, C., Brogioni, N., Vaselli, O., 2008. Formation of clinopyroxene + spinel and amphibole + spinel symplectites in coronitic gabbros from the Sierra de San Luis (Argentina): a key to post-magmatic evolution. *J. Metamorph. Geol.* 26, 759–774.
- Ellis, D., Green, D., 1979. An experimental study of the effect of Ca upon garnet-clinopyroxene Fe-Mg exchange equilibria. *Contrib. Miner. Petrol.* 71, 13–22.
- Gallien, F., Mogessie, A., Hauzenberger, C.A., Bjerg, E., Delpino, S., Castro De Machuca, B., 2012. On the origin of multi-layer coronas between olivine and plagioclase at the gabbro-granulite transition, Valle Fértil-La Huerta Ranges, San Juan Province, Argentina. *J. Metamorph. Geol.* 30, 281–302.
- Gardner, P., Robins, B., 1974. The olivine-plagioclase reaction: geological evidence from the Seiland petrographic province, Northern Norway. *Contrib. Miner. Petrol.* 44, 149–156.
- Gilley, L.D., Harrison, T.M., Leloup, P., Ryerson, F., Lovera, O.M., Wang, J.H., 2003. Direct dating of left-lateral deformation along the Red River shear zone, China and Vietnam. *J. Geophys. Res.: Solid Earth* 1978–2012, 108.
- Graham, C.M., Powell, R., 1984. A garnet-hornblende geothermometer: calibration, testing, and application to the Pelona Schist, Southern California. *J. Metamorph. Geol.* 2, 13–31.
- Green, D.H., Ringwood, A.E., 1967. An experimental investigation of the gabbro to eclogite transformation and its petrological applications. *Geochim. Cosmochim. Acta* 31, 767–833.
- Harley, S.L., 1984. The Solubility of Alumina in Orthopyroxene Coexisting with Garnet in  $\text{FeO}-\text{MgO}-\text{Al}_2\text{O}_3-\text{SiO}_2$  and  $\text{CaO}-\text{FeO}-\text{MgO}-\text{Al}_2\text{O}_3-\text{SiO}_2$ . *J. Petrol.* 25, 665–696.
- Harrison, T.M., Wenji, C., Leloup, P., Ryerson, F., Tappognon, P., 1992. An early Miocene transition in regime within the Red River fault zone, Yunnan, and its significance for Indo-Asian tectonics. *J. Geophys. Res.: Solid Earth* 1978–2012 (97), 7159–7182.
- Jolivet, L., Beyssac, O., Goffe, B., Avigad, D., Lepvrier, C., Maluski, H., Thang, T.T., 2001. Oligo-Miocene midcrustal subhorizontal shear zone in Indochina. *Tectonics* 20, 46–57.
- Kohn, M.J., Spear, F.S., 1989. Empirical calibration of geobarometers for the assemblage garnet + plagioclase + quartz. *Am. Miner.* 74, 77–84.
- Kohn, M.J., Spear, F.S., 1990. Two new geobarometers for garnet amphibolites, with applications to southeastern Vermont. *Am. Miner.* 75, 89–96.
- Koppers, A.A.P., 2002. ArArCALC-software for  $^{40}\text{Ar}/^{39}\text{Ar}$  age calculations. *Comput. Geosci.* 28, 605–619.
- Krogh, E.J., 1988. The garnet-clinopyroxene Fe-Mg geothermometer—a reinterpretation of existing experimental data. *Contrib. Miner. Petrol.* 99, 44–48.
- Leloup, P.H., Arnaud, N., Lacassin, R., Kienast, J.R., Harrison, T.M., Trong, T.T.P., Replumaz, A., Tappognon, P., 2001. New constraints on the structure, thermochronology, and timing of the Ailao Shan-Red River shear zone, SE Asia. *J. Geophys. Res.: Solid Earth* 106, 6683–6732.
- Leloup, P.H., Kienast, J.-R., 1993. High-temperature metamorphism in a major strike-slip shear zone: the Ailao Shan—Red River, People's Republic of China. *Earth Planet. Sci. Lett.* 118, 213–234.
- Leloup, P.H., Lacassin, R., Tappognon, P., Schärer, U., Zhong, D., Liu, X., Zhang, L., Ji, S., Trinh, P.T., 1995. The Ailao Shan-Red River shear zone (Yunnan, China), Tertiary transform boundary of Indochina. *Tectonophysics* 251, 3–84.
- Lin, T.-H., Chung, S.-L., Chiu, H.-Y., Wu, F.-Y., Yeh, M.-W., Searle, M.P., Iizuka, Y., 2012. Zircon U-Pb and Hf isotope constraints from the Ailao Shan-Red River shear zone on the tectonic and crustal evolution of southwestern China. *Chem. Geol.* 291, 23–37.
- Liu, F., Wang, F., Liu, P., Liu, C., 2013. Multiple metamorphic events revealed by zircons from the Diancang Shan-Ailao Shan metamorphic complex, southeastern Tibetan Plateau. *Gondwana Res.* 24, 429–450.
- Liu, P.-P., Zhou, M.-F., Chen, W.T., Boone, M., Cnudde, V., 2014a. Using multiphase solid inclusions to constrain the origin of the Baima Fe-Ti-(V) oxide deposit, SW China. *J. Petrol.* 55, 951–976.
- Liu, P.-P., Zhou, M.-F., Wang, C.Y., Xing, C.-M., Gao, J.-F., 2014b. Open magma chamber processes in the formation of the Permian Baima mafic-ultramafic layered intrusion, SW China. *Lithos* 184–187, 194–208.
- Liu, X.J., Liang, Q.D., Li, Z.L., Castillo, P.R., Shi, Y., Xu, J.F., Huang, X.L., Liao, S., Huang, W.L., Wu, W.N., 2017. Origin of Permian extremely high Ti/Y mafic lavas and dykes from Western Guangxi, SW China: Implications for the Emeishan mantle plume magmatism. *J. Asian Earth Sci.* 141, 97–111.
- Lu, Y.-J., Kerrich, R., McCuaig, T.C., Li, Z.-X., Hart, C.J., Cawood, P.A., Hou, Z.-Q., Bagas, L., Cliff, J., Belousova, E.A., 2013. Geochemical, Sr-Nd-Pb, and zircon Hf-O isotopic

- compositions of Eocene-Oligocene shoshonitic and potassic adakite-like felsic intrusions in western Yunnan, SW China: petrogenesis and tectonic implications. *J. Petrol.* 54, 1309–1348.
- Metcalfe, I., 1995. Gondwana dispersion and Asian accretion: An overview. *Gondwana dispersion and Asian accretion, Final Results Volume for IGC Project 321.*
- Okay, A.I., Xu, S., Sengor, A.C., 1989. Coesite from the Dabie Shan eclogites, central China. *Eur. J. Mineral.* 1, 595–598.
- Palin, R., Searle, M., Waters, D., Parrish, R., Roberts, N., Horstwood, M., Yeh, M.W., Chung, S.L., Anh, T., 2013. A geochronological and petrological study of anatetic paragneiss and associated granite dykes from the Day Nui Con Voi metamorphic core complex, North Vietnam: constraints on the timing of metamorphism within the Red River shear zone. *J. Metamorph. Geol.* 31, 359–387.
- Pang, K.N., Zhou, M.F., Lindsley, D., Zhao, D., Malpas, J., 2008. Origin of Fe-Ti oxide ores in mafic intrusions: Evidence from the Panzhihua intrusion, SW China. *J. Petrol.* 49, 295–313.
- Pang, K.N., Li, C.S., Zhou, M.F., Ripley, E.M., 2009. Mineral compositional constraints on petrogenesis and oxide ore genesis of the late Permian Panzhihua layered gabbroic intrusion, SW China. *Lithos* 110, 199–214.
- Paria, P., Bhattacharya, A., Sen, S., 1988. The reaction garnet + clinopyroxene + quartz = 2 orthopyroxene + anorthite: a potential geobarometer for granulites. *Contrib. Miner. Petrol.* 99, 126–133.
- Peng, H.B., 2009. The metallogenetic conditions of Dapo ore block of Mianhuadi titanomagnetite deposit in. *Yunnan Geol.* 28, 143–147 (in Chinese with English abstract).
- Powell, R., 1985. Regression diagnostics and robust regression in geothermometer/geo-barometer calibration: the garnet-clinopyroxene geothermometer revisited. *J. Metamorph. Geol.* 3, 231–243.
- Ravna, E.K., 2000. Distribution of  $\text{Fe}^{2+}$  and Mg between coexisting garnet and hornblende in synthetic and natural systems: an empirical calibration of the garnet-hornblende Fe-Mg geothermometer. *Lithos* 53, 265–277.
- Schärer, U., Tappognier, P., Lacassin, R., Leloup, P.H., Dalai, Z., Shaocheng, J., 1990. Intraplate tectonics in Asia: a precise age for large-scale Miocene movement along the Ailao Shan-Red River shear zone, China. *Earth Planet. Sci. Lett.* 97, 65–77.
- Schärer, U., Zhang, L.-S., Tappognier, P., 1994. Duration of strike-slip movements in large shear zones: the Red River belt, China. *Earth Planet. Sci. Lett.* 126, 379–397.
- Schoenbohm, L.M., Burchfiel, B.C., Liangzhong, C., Jiyun, Y., 2006. Miocene to present activity along the Red River fault, China, in the context of continental extrusion, upper-crustal rotation, and lower-crustal flow. *Geol. Soc. Am. Bull.* 118, 672–688.
- Searle, M.P., 2006. Role of the Red River Shear zone, Yunnan and Vietnam, in the continental extrusion of SE Asia. *J. Geol. Soc.* 163, 1025–1036.
- Searle, M.P., Yeh, M.-W., Lin, T.-H., Chung, S.-L., 2010. Structural constraints on the timing of left-lateral shear along the Red River shear zone in the Ailao Shan and Diancang Shan Ranges, Yunnan, SW China. *Geosphere* 6, 316–338.
- Smithies, R., Bagas, L., 1997. High pressure amphibolite-granulite facies metamorphism in the Paleoproterozoic Rudall Complex, central Western Australia. *Precambr. Res.* 83, 243–265.
- Song, X.-Y., Qi, H.-W., Hu, R.-Z., Chen, L.-M., Yu, S.-Y., Zhang, J.-F., 2013. Formation of thick stratiform Fe-Ti oxide layers in layered intrusion and frequent replenishment of fractionated mafic magma: evidence from the Panzhihua intrusion, SW China. *Geochem. Geophys. Geosyst.* 14, 712–732.
- Steiger, R.H., Jäger, E., 1977. Subcommission on geochronology: convention on the use of decay constants in geo-and cosmochronology. *Earth Planet. Sci. Lett.* 36, 359–362.
- Tappognier, P., Lacassin, R., Leloup, P.H., Schärer, U., Dalai, Z., 1990. The Ailao Shan/Red River metamorphic belt: tertiary left-lateral shear between Indochina and South China. *Nature* 343, 431.
- Tappognier, P., Peltzer, G., Le Dain, A., Armijo, R., Cobbold, P., 1982. Propagating extrusion tectonics in Asia: new insights from simple experiments with plasticine. *Geology* 10, 611–616.
- Wang, C.Y., Zhou, M.-F., 2013. New textural and mineralogical constraints on the origin of the Hongge Fe-Ti-V oxide deposit, SW China. *Miner. Deposita* 48, 787–798.
- Wang, C.Y., Zhou, M.-F., Qi, L., 2007. Permian flood basalts and mafic intrusions in the Jinping (SW China)-Song Da (northern Vietnam) district: Mantle sources, crustal contamination and sulfide segregation. *Chem. Geol.* 243, 317–343.
- Wang, F., Jourdan, F., Lo, C.-H., Nomade, S., Guillou, H., Zhu, R., Yang, L., Shi, W., Feng, H., Wu, L., 2014. YBCS sandine: a new standard for  $^{40}\text{Ar}/^{39}\text{Ar}$  dating. *Chem. Geol.* 388, 87–97.
- Wang, F., Liu, F., Liu, P., Shi, J., Cai, J., 2016. Petrology, geochemistry, and metamorphic evolution of meta-sedimentary rocks in the Diancang Shan-Ailao Shan metamorphic complex, Southeastern Tibetan Plateau. *J. Asian Earth Sci.* 124, 68–93.
- Xu, Y.-G., Chung, S.-L., Jahn, B.-M., Wu, G., 2001. Petrologic and geochemical constraints on the petrogenesis of Permian-Triassic Emeishan flood basalts in southwestern China. *Lithos* 58, 145–168.
- Yeh, M.-W., Lee, T.-Y., Lo, C.-H., Chung, S.-L., Lan, C.-Y., Anh, T.T., 2008. Structural evolution of the Day Nui Con Voi metamorphic complex: implications on the development of the Red River Shear Zone, Northern Vietnam. *J. Struct. Geol.* 30, 1540–1553.
- Yeh, M.-W., Wintsch, R., Liu, Y.-C., Lo, C.-H., Chung, S.-L., Lin, Y.-L., Lee, T.-Y., Wang, Y.-C., Stokes, M., 2014. Evidence for cool extrusion of the North Indochina block along the Ailao Shan Red River shear zone, a Diancang Shan perspective. *J. Geol.* 122, 567–590.
- York, D., 1969. Least squares fitting of a straight line with correlated errors. *Earth Planet. Sci. Lett.* 5, 320–324.
- Zhang, X.R., Shi, R.D., Huang, Q.S., Liu, D.L., Cidan, S.L., Yang, J.S., Ding, L., 2010. Finding of high-pressure mafic granulites in the Amdo basement, central Tibet. *Chin. Sci. Bull.* 55, 3694–3702.
- Zhang, X.R., Shi, R.D., Huang, Q.S., Liu, D.L., Gong, X.H., Chen, S.S., Wu, K., Yi, G.D., Sun, Y.L., Ding, L., 2014. Early Jurassic high-pressure metamorphism of the Amdo terrane, Tibet: constraints from zircon U-Pb geochronology of mafic granulites. *Gondawana Res.* 26, 975–985.
- Zhang, L.-S., Schärer, U., 1999. Age and origin of magmatism along the Cenozoic Red River shear belt, China. *Contrib. Miner. Petrol.* 134, 67–85.
- Zhao, G., Cawood, P.A., Wilde, S.A., Lu, L., 2001. High-pressure granulites (retrograded eclogites) from the Hengshan Complex, North China Craton: petrology and tectonic implications. *J. Petrol.* 42, 1141–1170.
- Zhao, G., Cawood, P.A., Wilde, S.A., Sun, M., Lu, L., 2000. Metamorphism of basement rocks in the Central Zone of the North China Craton: implications for Paleoproterozoic tectonic evolution. *Precambr. Res.* 103, 55–88.
- Zhao, G., Sun, M., Wilde, S.A., 2003. Major tectonic units of the North China Craton and their Paleoproterozoic assembly. *Sci. China, Ser. D Earth Sci.* 46, 23–38.
- Zhou, M.-F., Chen, W.T., Wang, C.Y., Prevec, S.A., Liu, P.P., Howarth, G.H., 2013. Two stages of immiscible liquid separation in the formation of Panzhihua-type Fe-Ti-V oxide deposits, SW China. *Geosci. Front.* 4, 481–502.